Perturbation theory for metal pad roll instability in cylindrical reduction cells

Herreman, W.; Nore, C.; Guermond, J.-L.; Cappanera, L.; Weber, N.; Horstmann, G. M.;

Metal pad roll instability in cylindrical reduction cells : perturbation theory vs. direct numerical simulations

W. Herreman* and C. Nore

LIMSI, CNRS, Université Paris-Sud, Université Paris-Saclay, Orsay, F-91405, France

J.-L. Guermond

TAMU, Texas A&M, College station, USA

L. Cappanera

Department of Computational and Applied Mathematics,
Rice University, 6100 Main St., Houston, TX 77005-1827, USA

N. Weber and G. M. Horstmann

HZDR, Dresden, Germany
(Dated: July 26, 2018)

We formulate a precise theoretical model for the linear instability of gravity waves in a cylindrical reduction cell. This model is new and complete because it overcomes basically all assumptions that are usually made in metal pad roll theory: it is non-shallow, includes viscous and magnetic damping, includes interfacial tension, is valid for any combination of metal and captures bot horizontal and vertical magnetic field effects. We confront the calculated viscous damping rates to experimental measures and the linear stability theory to direct numerical simulations done with two independent numerical solvers SFEMaNS and OpenFOAM and find excellent agreement.

---

* wietze@limsi.fr; http://perso.limsi.fr/wietze/

I. INTRODUCTION

The metal pad roll instability is a magnetohydrodynamical phenomenon that disturbs the production of Aluminium in Hall-Heroult reduction cells. A small background magnetic field that reigns in the Aluminium factory can interact with the electrolysis current to create a magnetic coupling between transverse gravity waves. Above a threshold electrolysis current or beneath a minimal Cryolite layer depth, this coupling can drive rotating gravity waves on the interface between the Cryolite and the Aluminium. This is undesired as such waves can cause short-circuits between the Carbon anodes and the Aluminium bath which makes the industrial process less efficient.

The first physical descriptions of the metal pad roll instability go back to [1, 2], but many other models have been developed in order to map out the metal pad roll instability in Aluminium reduction cells [3–11]. With their very shallow character (several meters in lateral extend, only a few centimeters in height), Hall-Heroult cells can be accurately modeled using shallow layer expansions, (see [8]). Most often they are so large that all capillary, viscous and magnetic dissipation effects are ignored at first order and inviscid instability criteria then take the form of $\beta > \beta_c$. Here β is a non-dimensional number defined below and β_c only depends on the geometry of the cell and of the vertical magnetic field.

Although linear theory can explain the physical origin of the instability it is not adapted to predict the nonlinear development or the amplitudes of the destabilized waves. Several two-dimensional and nonlinear shallow models have therefore been derived and perfected over the years to account for the complex magnetic fields that may occur in industrial cell configurations [8, 12–14]. These models are so economical to run that they can effectively be used to design stabler reductions cells. As numerical resources increased over time, it also became possible to do direct numerical simulations of the full three-dimensional nonlinear dynamics of reduction cells. This approach is much more computationally demanding and was initiated by [15–17] who used a finite element ALE-method. Not much later, commercial codes ANSYS & CFX were interfaced in [18, 19]. A finite volume level-set method was developed by [20, 21] and a finite-element method with mobile grid was developed in [22–24]. Each of these advanced numerical tools have been carefully tested and applied to Aluminium reduction cells, but true quantitive comparisons between direct numerical simulations and theoretical models remain relatively scarce. This for several reasons: (i) theoretical models often ignore dissipative effects, which cannot be ignored in DNS. (ii) most theory is dedicated to shallow cells but not all the direct numerical simulations are done in shallow cells. (iii) many direct numerical simulations focus on realistic cell geometries for which no simple theoretical model is available. The result is that most metal pad roll theory is rather disconnected from what happen in the direct numerical simulations.

This brings us to the *first motivation* for this study. We believe that there are too few clear overlaps between theory and direct numerical simulations, making it difficult to estimate what theoretical mechanisms are operational in which simulations. In this article, we aim to provide a complete description of the metal pad roll phenomenon, that combines theory, direct numerical simulations and even some (hydrodynamical) experiments.

Our *second motivation* for this study is to be found in the context of liquid metal battery fluid dynamics. In recent times, the metal pad roll phenomenon has also been studied in these three-layer systems [35–37, 48–51]. Although we can imagine that future large scale liquid battery systems may become as shallow as Hall-Heroult reduction cells, present day prototypes are laboratory scale and certainly not always shallow. To interpret the numerical simulations of [35–37] a new theory that is non-shallow, viscous and includes magnetic damping effects and capilarity seems necessary. But first we needed to learn how to manage only two fluid layers.

We finally also have a *third motivation* which is more a numerical one. All the numerical simulations presented here will be done here with two independent multiphase MHD solvers, SFEMaNS and OpenFOAM that arrive as relatively new players in the area of metal pad roll simulations. Our first solver SFEMaNS is being developed since 2001 and was initially designed to solve MHD problems in axisymmetric geometries. The discretization is done using Fourier expansions in the azimuthal direction and finite elements in the (r, z)-plane. First designed to study dynamo problems in axisymmetric domains (see [25, 26]), the code has been modified to account for non-axisymmetric geometries [27]. More recently, it has been further upgraded to solve multiphase MHD problems using a level-set method that is fully explained in [28]. In [29] we used SFEMaNS to study the Tayler instability in liquid metal battery systems and some preliminary simulations on metal pad roll instability are mentioned in [28]. Our second solver is based on the finite volume library OpenFOAM [30]. Since 2010 this code is capable of solving quasi-static MHD and it was used to study Tayler instability [31, 32] and electrovortex flow [33, 34]. A volume-of-fluid model is used to implement multiple liquid phases and has allowed to perform several studies on metal pad roll instability in liquid metal batteries [35–37]. Although both codes have been used in previous studies, we still haven't passed a fine non-axisymmetric benchmark involving both codes at the same time. We found that the metal pad roll instability is perfect for this and in order to measure the true numerical cost of a well-resolved simulation we evidently needed a precise theoretical model to compare with.

In §2, we formulate our theoretical model for the linear instability of gravity waves in a cylindrical reduction cell. Cylindrical cells are perhaps not realistic for industrial devices, but they have been studied before in theory [9, 10] and
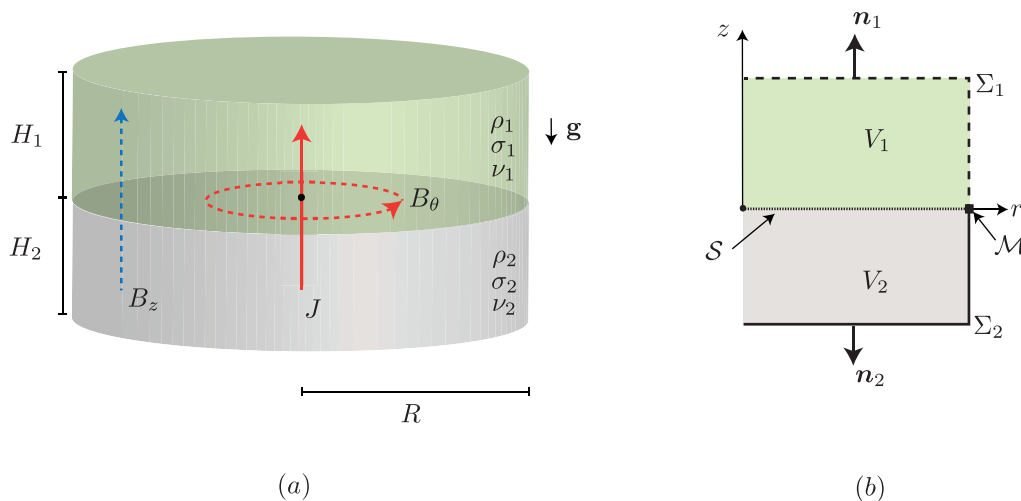
FIG. 1. Sketch of cylindrical model cell and notations. (a) Two fluid layers with different densities ρ_1, ρ_2 and respective heights H_1, H_2 are stably superposed in a cylindrical container of radius R due to gravity $\boldsymbol{g}$. The layers have different electrical conductivity and kinematic viscosity denoted as σ_i, ν_i, $i = 1, 2$ A vertical electrical current runs $J\boldsymbol{e}_z$ through the cell (red full line) which generates an azimuthal magnetic field B_θ (red dashed line). We also suppose a homogenous and vertical background magnetic field B_z (bleu dashed line). (b) We use cylindrical coordinates (r, θ, z) and denote V_i, $i = 1, 2$ for both fluid regions. Σ_i, $i = 1, 2$ refer to the rigid boundaries, $\mathcal{S}$ to the free interface at rest, $\mathcal{M}$ to the meniscus region. $\boldsymbol{n}_i$ is the external normal on both fluid regions.

in numerical simulations [15, 23]. Our model is new and complete because it overcomes basically all assumptions that are usually made in metal pad roll theory: it is non-shallow, includes magnetic damping, includes interfacial tension, is valid for any combination of conducting fluids and includes viscous damping. The price to pay for this generality is that the theory is a perturbation theory with limited range of validity. We will demonstrate that even large cells can be unstable in the range covered by our theory, but the true novelties will be visible in small cells, that are much more prone to viscous and magnetic damping and capillary effects.

In §3, we discuss some purely hydrodynamical experiments that serve as tests for the theoretically calculated viscous damping rates. These datapoints appear as interesting by-product of a novel experimental study on orbital sloshing in two and three layer fluid systems that is to appear [38]. Orbital sloshing corresponds to prescribing a circular translation to a container (used to swirl for exemple a glass of wine) and it drives exactly the same wave mode that is commonly associated with the metal pad roll instability. In this experimental study, we employed the working fluids Paraffinum Perliquidum and Wacker® silicone oil AK 35 forming a stable interface, which fulfills in good approximation the idealized free-moving contact line boundary condition assumed in our theory. We compare measured interfacial damping rates for different layer heights with the theoretical predictions and found very good agreement.

In §4, we apply the theoretical model to two different reduction cells, a small laboratory-scale cylindrical reduction cell and a large industrial scale cell. For the large cells, we limit ourselves to applying the theoretical model, demonstrating here that perturbation methods can be used even in such huge cells. The small cell is more hypothetical and was briefly discussed in [22, 23] as a test-case for their multiphase MHD solver. With a radius of only $R = 0.035$ m, the small lab-scale cell can only become unstable when very large ambient magnetic fields are present, far above what we can have in Aluminium factories, but close to what we had in the experiments of [39, 40]. The biggest advantage and interest of the small cell geometry is that very well resolved direct numerical simulations are amenable allowing to compare gravity wave frequencies, viscous dissipation rates, magnetic dissipation rates and finally metal pad roll instability growth rates for various parameter sets and waves and using different numerical resolutions.

In §5, we conclude and discuss some perspectives of our study.

II. THEORETICAL ANALYSIS

A. Cylindrical reduction cell at equilibrium

The cylindrical cell is sketched in figure 1. We align the axis of symmetry with the z-axis of a cylindrical coordinate system (r, θ, z) with unit vectors $(\boldsymbol{e}_r, \boldsymbol{e}_\theta, \boldsymbol{e}_z)$. At equilibrium, the Cryolite and Aluminium layers (subscripts $i = 1, 2$) occupy the volumes

$$\begin{aligned}
\mathcal{V}_1 &: (r, \theta, z) \in [0, R] \times [0, 2\pi[\times [0, H_1] \\
\mathcal{V}_2 &: (r, \theta, z) \in [0, R] \times [0, 2\pi[\times [-H_2, 0]
\end{aligned} \tag{1}$$

R is the radius of the cell and H_i is the height of both layers. We denote δV_i the boundary of each fluid domain and split $\delta V_i = \Sigma_i \cup \mathcal{S}$, with Σ_i the rigid boundary and $\mathcal{S}$ the interface at rest. $\boldsymbol{n}_i$ is the outward normal on δV_i.

The electrical conductivity, density, kinematic viscosity of both fluids are denoted by σ_i, ρ_i, ν_i. The surface tension of the interface in between both fluids is denoted by $\gamma_{1|2}$. We suppose that the interface connects with a contact angle of 90° to the lateral wall and that it is not pinned. This is a strong hypothesis that is necessary to allow for an equilibrium state with a flat interface. Capillarity is not often considered in metal pad roll theory since the capillary length is always very small compared to the system size in realistic cells. In small cells, capillarity may be relevant and since it may be easily included in the model, we decide to consider its effect.

If the cell is at (magnetohydrodynamical) equilibrium, both fluids are at rest. The fluids are subject to gravity $\boldsymbol{g} = -g\,\boldsymbol{e}_z$. A homogenous electrical current density $\boldsymbol{J} = J\boldsymbol{e}_z$ runs through the cell (in reduction cells, $J < 0$ always). A magnetic field $\boldsymbol{B} = B_\theta \boldsymbol{e}_\theta + B_z \boldsymbol{e}_z$ is present. The azimuthal (or horizontal) field $B_\theta = \mu_0 Jr/2$ increases radially and is self-generated by the electrical current in the cell. The vertical component of the magnetic field B_z is supposed constant and entirely due to an external source. The defined state is a magnetohydrodynamical equilibrium configuration if the hydrodynamic pressure is $P_i = P_* - \rho_i gz - \mu_0 J^2 r^2/4$ and the electrical potential is $\Phi_i = \Phi_* - Jz/\sigma_i$ with P_*, Φ_* arbitrary and constant offsets.

B. Linearized problem in the quasi-static limit

From many previous studies we know that the defined equilibrium state can become unstable. We perform a linear stability analysis that takes into account viscous dissipation, magnetic dissipation, surface tension, without making a shallow layer approximation. We start by linearizing the governing equations about the equilibrium state. Denoting $B = \max(\mu_0 JR, B_z)$ the typical scale for the magnetic field strength, we will suppose that the Lundquist numbers Lu_i in both layers remain very low:

$$\mathrm{Lu}_i = \sigma_i \mu_0 BR / \sqrt{\rho_i \mu_0} \ll 1 \tag{2}$$

This hypothesis allows us to use the quasi-static approximation of MHD, in which the electrical field derives from the electrical potential. Denoting with $(\boldsymbol{u}_i, p_i, \boldsymbol{b}_i, \boldsymbol{j}_i, \varphi_i)$ perturbations for flow, pressure, magnetic induction, current density and electrical potential, we find the linearized perturbation equations of the magnetohydrodynamical stability problem as

$$\rho_i \partial_t \boldsymbol{u}_i + \boldsymbol{\nabla} p_i = \boldsymbol{J} \times \boldsymbol{b}_i + \boldsymbol{j}_i \times \boldsymbol{B} + \rho_i \nu_i \boldsymbol{\nabla}^2 \boldsymbol{u}_i \tag{3a}$$

$$\boldsymbol{\nabla} \cdot \boldsymbol{u}_i = 0 \tag{3b}$$

$$\boldsymbol{j}_i = \sigma_i(-\boldsymbol{\nabla}\varphi_i + \boldsymbol{u}_i \times \boldsymbol{B}) \ , \ \boldsymbol{\nabla} \cdot \boldsymbol{j}_i = 0 \tag{3c}$$

$$\boldsymbol{\nabla} \times \boldsymbol{b}_i = \mu_0 \boldsymbol{j}_i \ , \ \boldsymbol{\nabla} \cdot \boldsymbol{b}_i = 0 \tag{3d}$$

for $i = 1, 2$. The essential inviscid hydrodynamical boundary condition on the rigid boundaries Σ_i is that of impermeability

$$\boldsymbol{u}_i \cdot \boldsymbol{n}_i = 0|_{\Sigma_i} \tag{4}$$

to which we must add $\boldsymbol{u_i} \times \boldsymbol{n}_i = 0|_{\Sigma_i}$ in viscous fluids. On the interface $\mathcal{S}$, that we locate at $z = \eta(r, \theta, t)$, the essential inviscid boundary conditions are

$$\partial_t \eta = u_{1,z}|_{z=0} \tag{5a}$$

$$\partial_t \eta = u_{2,z}|_{z=0} \tag{5b}$$

$$-\gamma_{1|2}\boldsymbol{\nabla}^2\eta + (\rho_2 - \rho_1)g\eta = p_2|_{z=0} - p_1|_{z=0} \tag{5c}$$

In viscous flows, we must add the continuity of tangential flow-components and the continuity of tangential viscous stresses (explicit formulae are not required in the article). For what concerns the electrical boundary conditions on the rigid boundaries Σ_i, we will suppose

$$j_{1,r}|_{r=R} = 0 \tag{6a}$$
$$j_{2,r}|_{r=R} = 0 \tag{6b}$$
$$\varphi_1|_{z=H_1} = 0 \tag{6c}$$
$$j_{2,z}|_{z=-H_2} = 0 \tag{6d}$$

The cylindrical wall is always isolating. The top boundary is treated as an electrical contact with a perfect conductor (iso-potential surface), mimicking the fact that the Carbon anode is a very good conductor compared to Cryolite. The bottom boundary is treated as an electrical contact with an isolating material, mimicking the fact that the steel cathode is weakly conducting compared to the liquid Aluminium. These idealized boundary conditions have been used by many authors and are relevant to reduction cells. On the free interface $\mathcal{S}$, we need to satisfy

$$0 = j_{1,z}|_{z=0} - j_{2,z}|_{z=0} \tag{7a}$$
$$J(\sigma_2^{-1} - \sigma_1^{-1})\eta = \varphi_2|_{z=0} - \varphi_1|_{z=0} \tag{7b}$$

Equation (7b) plays an essential role for the metal pad roll instability, since it expresses how electrical potential perturbations φ_i (and so currents $\boldsymbol{j}_i$) relate to interface movements. Finally, for the magnetic induction that is driven by the electrical currents, we will suppose the following simplifying boundary condition on the cylindrical boundary

$$\boldsymbol{e}_r \times \boldsymbol{b}_i|_{r=R} = 0 \tag{8}$$

Boundary conditions at other places are not required in the analysis. This condition is simplifying as it will allow us to avoid the explicit calculation of the magnetic field, which never is an easy task in finite fluid domains surrounded by a current-free exterior. A similar boundary condition was used in a previous study [29] on the Tayler instability and it had little impact on that instability.

The linearized problem is now completely defined and so we can search for linear eigenmodes. Due to the stationarity of the equilibrium state, we can search for fundamental solutions with a simple exponential time-dependence. More precisely, if f represents any of the relevant fields or components, we can propose

$$f = \hat{f}e^{st} \tag{9}$$

and find the admissible (complex) eigenmodes $\hat{f}$ and (complex) eigenvalues $s \in \mathbb{C}$. We can call $\mathrm{Re}(s)$ the growth rate and $\mathrm{Im}(s)$ the frequency. If $\mathrm{Re}(s) > 0$, the eigenmode is linearly unstable and if $\mathrm{Im}(s) \neq 0$ the solution is wave-like.

Using a numerical approach it is possible to solve this linear eigenvalue problem exactly. In the following parts of this theoretical section, we use a perturbative approach. We model how free inviscid gravity waves are weakly stabilized, destabilized or detuned in frequency, by magnetohydrodynamical and viscous effects that are supposed to be weak enough so that the waves conserve their structural integrity.

C. Free inviscid gravito-capillary waves

Our perturbative approach expands on the free inviscid gravito-capillary waves that exist as the family of eigensolutions, in absence of electrolysis current ($J = 0$), vertical magnetic field ($B_z = 0$) and without viscosity ($\nu = 0$). In that case, we can propose a hydrodynamical solution

$$[\boldsymbol{u}_i, p_i, \eta] = [\widehat{\boldsymbol{u}}_i, \widehat{p}_i, \widehat{\eta}]\, e^{\mathrm{i}\omega t} \tag{10}$$

to the linearized problem defined above. The hydrodynamical fields $\widehat{\boldsymbol{u}}_i, \widehat{p}_i, \widehat{\eta}$ correspond to the classical potential wave solution (see [41]):

$$
\begin{bmatrix} \widehat{\boldsymbol{u}}_i \\ \widehat{p}_i \\ \widehat{\eta} \end{bmatrix}
=
\begin{bmatrix} \boldsymbol{\nabla}\widehat{\phi}_i \\ -\rho_i(\mathrm{i}\omega)\widehat{\phi}_i \\ \partial_z\widehat{\phi}_i/(\mathrm{i}\omega) \end{bmatrix}
\quad\text{with}\quad
\begin{bmatrix} \widehat{\phi}_1 \\ \widehat{\phi}_2 \\ \widehat{\eta} \end{bmatrix}
= A
\begin{bmatrix} \cosh(k(z - H_1))/\sinh(kH_1) \\ -\cosh(k(z + H_2))/\sinh(kH_2) \\ \mathrm{i}k/\omega \end{bmatrix}
J_m(kr)\, e^{\mathrm{i}m\theta} \tag{11}
$$

The number A is arbitrary here and has the dimension of hydrodynamic potential. The functions J_m are Bessel-functions, $m \in \mathbb{Z}$ is the azimuthal wavenumber and k is a radial wavenumber that can take any value

$$k = \kappa_{mn}/R \quad,\quad J'_m(\kappa_{mn}) = 0 \tag{12}$$

Here κ_{mn} is a notation for the n-th zero of the derivative of the Bessel function J_m. Only these choices of k can assure that $u_r|_{r=R} = 0$ is satisfied. The natural frequency ω of the (free) waves is

$$\omega = \pm \sqrt{\frac{(\rho_2 - \rho_1)gk + \gamma_{1|2}k^3}{\rho_2 \tanh^{-1}(kH_2) + \rho_1 \tanh^{-1}(kH_1)}} \tag{13}$$

and may be either positive or negative for fixed m. The solution presented here (see (10)) has a simple harmonic form, but the real flow is always real-valued. Taking the real part of (10), one finds rotating waves with positive rotation speed if $m\omega < 0$ (anti-clockwise when seen from above) and negative rotation speed if $m\omega > 0$ (clockwise when seen from above). Two oppositely rotating waves can also be superposed to give standing waves.

D. Sufficient conditions to apply perturbation methods

Perturbation methods may only be used when the Lorentz force and the viscous forces appear as small perturbations in the momentum balance. Symbolically, this means that

$$[\boldsymbol{J} \times \boldsymbol{b}_i], [\boldsymbol{j}_i \times \boldsymbol{B}], [\rho_i \nu_i \boldsymbol{\nabla}^2 \boldsymbol{u}_i] \ll [\rho_i \partial_t \boldsymbol{u}_i], [\boldsymbol{\nabla} p_i] \tag{14}$$

in terms of orders of magnitude (denoted using square brackets). This sets limitations on the parameter space that can be explored and we want to estimate these limits here.

For simplicity, we assume $J, B, \omega \geq 0$ to avoid the use of absolute values. We use $[\boldsymbol{x}] = R$ as space scale rather than k^{-1} since this is more explicit (and anyway similar to k^{-1} for long wave-length waves). We denote $[\boldsymbol{u}_i] = U$ the velocity scale that is arbitrary in this linear approach. For hydrodynamic waves, we can estimate

$$[\rho_i \partial_t \boldsymbol{u}_i] \sim \rho_i \omega U \quad , \quad [p_i] \sim \rho_i \omega R U \tag{15}$$

The viscous term has an order of magnitude

$$[\rho_i \nu_i \boldsymbol{\nabla}^2 \boldsymbol{u}_i] \sim \rho_i \nu_i U / R^2 \tag{16}$$

We introduce B as the order of magnitude of the imposed magnetic field

$$[\boldsymbol{B}] \sim B = \begin{cases} \mu_0 J R & \longrightarrow \quad \text{azimuthal} \\ B_z & \longrightarrow \quad \text{vertical} \end{cases} \tag{17}$$

We can use two independent estimates, related to either the azimuthal or to the vertical magnetic field. From Ohm's law (3c), we then estimate the magnitude of the induction term as

$$[\sigma_i \boldsymbol{u}_i \times \boldsymbol{B}] \sim \sigma_i U B \tag{18}$$

Still in Ohm's law (3c), the electrical potential term may have the same order of magnitude, but interface deformations caused by waves can also lead to a different magnitude that can be estimated from boundary conditions (5a), (5b) and (7b). This yields the following two different estimates for the electrical current density

$$[\boldsymbol{j}_i] \sim [-\sigma_i \boldsymbol{\nabla} \varphi_i] \sim \begin{cases} JU/\omega R & \longrightarrow \quad \text{interface deformations} \\ \sigma_i U B & \longrightarrow \quad \text{induction by the flow} \end{cases} \tag{19}$$

Using Ampère's law (3d), we can calculate the associated magnetic field perturbation magnitudes

$$[\boldsymbol{b}_i] \sim \begin{cases} \mu_0 JU/\omega \\ \mu_0 \sigma_i U R B \end{cases} \tag{20}$$

All orders of magnitude of the different fields have now been estimated so we can now re-express the initial inequalities (14). The trivial but sufficient condition to model viscous effects perturbatively is

$$[\rho_i \nu_i \boldsymbol{\nabla}^2 u_i] \ll [\rho_i \partial_t \boldsymbol{u}_i] \quad \Leftrightarrow \quad Re_i = \frac{\omega R^2}{\nu_i} \gg 1 \tag{21}$$

which we recognize as a contraint on Reynolds numbers based on the properties of the wave. A set of sufficient conditions that allow to model the effect of the Lorentz-force using perturbation methods is then

$$[\boldsymbol{J} \times \boldsymbol{b}_i] \ll [\rho_i \partial_t \boldsymbol{u}_i] \quad \Leftrightarrow \quad \begin{cases} \dfrac{\mu_0 J^2}{\rho_i \omega^2} \ll 1 \\[3mm] \dfrac{\mu_0 \sigma_i J R B}{\rho_i \omega} \ll 1 \end{cases} \tag{22a}$$

$$[\boldsymbol{j}_i \times \boldsymbol{B}] \ll [\rho_i \partial_t \boldsymbol{u}_i] \quad \Leftrightarrow \quad \begin{cases} \dfrac{J B}{\rho_i \omega^2 R} \ll 1 \\[3mm] \dfrac{\sigma_i B^2}{\rho_i \omega} \ll 1 \end{cases} \tag{22b}$$

Each time we have two estimates that relate to the two choices (19) we can make. We will suppose that these a-priori sufficient conditions (21) and (22) are verified. However, it is impossible to evaluate how necessary they are. A posteriori, when we have calculated the growth rates, we will be able to provide more reasonable estimates of the domain of validity of our perturbative model.

E. Simplifying assumptions in other studies on metal pad roll instability

Most existing theoretical work on metal pad roll instabilities has not been done with a perturbative approach, but other simplifying assumptions have frequently been made. Here we discuss these assumptions and their impact, to be able to situate how the present model is similar or different.

A first frequently made assumption is that of shallow fluid layers. This is very relevant to model the long wavelength waves that occur in realistic Hall-Heroult cells, that are very wide ($4-10$ m in lateral extend) but very shallow ($5-30$ cm high). The shallow layer hypothesis is however not so adapted to the small laboratory scale reduction cells studied numerically in this article and in [22, 23], nor to the experimental set-up of [39, 40], nor to the metal pad roll studies in liquid metal batteries of [35, 36]. We do not use the shallow approximation in our theory, but will expand our formula in this limit in order to be able to compare to the existing models of [9, 10].

A second frequent assumption is that of inviscid fluids. This is simplifying for the analysis and since viscous effects are not crucial to the physical mechanism of the metal pad roll instability, the only thing that is missed is a dissipative mechanism. In realistic cells, far from the instability threshold, viscosity is less important, but in small cells near the instability threshold, one must account for the viscous damping in order to have a precise theory. We will provide a explicit formula for the viscous damping rate of waves in cylindrical geometry.

A third assumption relates to Ohm's law. A very popular assumption in metal pad roll theory is

$$[\sigma_i \boldsymbol{u}_i \times \boldsymbol{B}] \ll [-\sigma_i \boldsymbol{\nabla} \varphi_i] \quad \Leftrightarrow \quad \frac{\sigma_i \omega R B}{J} \ll 1 \tag{23}$$

and when this inequality is satisfied, the dominant contribution to the electrical current perturbation is caused by interface movements rather than by field induction in the bulk of the flow. In this limit, the magneto-static approximation

$$\boldsymbol{j}_i \approx -\sigma_i \boldsymbol{\nabla} \varphi_i \tag{24}$$

may be used as a first order approximation, rather than the quasi-static Ohm's law (3c). Physically, we then calculate the current density perturbation as if the metal slabs were solids at rest. This hypothesis is quite well adapted to realistic Hall-Heroult cells, in particular since $B = B_z$ always remains fairly low (~ 1mT). For what concerns the horizontal magnetic field $B = \mu_0 J R$, it seems more easy to violate

$$\sigma_i \mu_0 \omega R^2 \ll 1 \tag{25}$$

in large cells. Note that this number looks as a magnetic Reynolds number based on wave-speed. The physical effect of the term $\sigma_i \boldsymbol{u}_i \times B_z \boldsymbol{e}_z$ is well known: it creates a magnetic damping and in [42] this damping was calculated in rectangular fluid containers with isolating walls. The physical effect of the term $\sigma_i \boldsymbol{u}_i \times (\mu_0 J r/2) \boldsymbol{e}_\theta$ is less well described. It may be stabilizing but it can also be destabilizing as we know from the Tayler instability [29]. Below we will study the effect of both terms and for the magnetic damping due to the vertical magnetic field, we will provide an explicit formula.

A fourth frequently made assumption is that

$$[\boldsymbol{J} \times \boldsymbol{b}_i] \ll [\boldsymbol{j}_i \times \boldsymbol{B}] \quad \Leftrightarrow \quad \frac{\mu_0 JR}{B} \ll 1 \tag{26}$$

which allows to approximate

$$\text{Lorentz force}_i \approx \boldsymbol{j}_i \times \boldsymbol{B} \tag{27}$$

The induced field $\boldsymbol{b}_i$ does not need to be calculated which is very practical as $\boldsymbol{b}_i$ is never easy to compute in finite fluid domains with realistic boundary conditions. Considering the definition (17) of B, this condition $\mu_0 JR/B \ll 1$ is only realizable when the vertical magnetic field dominates the horizontal field, rarely the case in industrial-size cells. In [43], the effect of the term $\boldsymbol{J} \times \boldsymbol{b}_i$ was studied and it was shown to have little impact on the instability. In the following, we will not ignore this term and find that it mainly modifies the frequency of waves.

A fifth assumption is that capillarity is not important. For gravity waves, this means that

$$kl_c \ll 1 \quad , \quad l_c = \sqrt{\frac{\gamma_{1|2}}{(\rho_2 - \rho_1)g}} \tag{28}$$

in other words, the capilllary length l_c needs to much smaller than the wavelength $2\pi/k$. This condition is very well verified by long-wavelength waves in industrial Hall-Heroult cells. In small cells, it will be harder to hold this inequality and surface tension will modify the frequency of the waves and the metal pad roll instability significantly. Therefore, we include surface tension in this model.

Finally, a sixth assumption is that the electrical conductivity of both layers is very different:

$$\frac{\sigma_1}{\sigma_2} \ll 1 \tag{29}$$

This is more a fact than an assumption in Hall-Heroult cells. Combined with the shallow nature of the cells and the electrical top and bottom boundary conditions, it allows to estimate that currents are mainly vertical in the electrolyte and mainly horizontal in the Aluminium. As a result, metal pad roll instability growth rates do not depend on the electrical conductivity of the layers. In this article, we will find both σ_1 and σ_2 in our growth rate formula. This allows us to explore how strongly one can relax conductivities of both layers in direct numerical simulations, since weaker conductivity jumps are more easily manageable for multiphase MHD codes.

F. Perturbative calculation of growth rates and frequency shifts

In this section, we find a theoretical expression for the complex eigenvalue s that characterizes the exponential behavior ($\sim \exp(st)$) of the linear eigenmode. We will model the effect of the Lorentz-force and viscosity perturbatively and since these calculations are rather technical it is useful to give a quick idea of our purpose. The theoretical expression for s will be split as

$$s = i\omega + \underbrace{(\lambda + i\delta)}_{\alpha} \tag{30}$$

Here ω is the inviscid gravity wave frequency and α is a small complex shift induced by Lorentz and viscous forces. We define $\lambda = \text{Re}(\alpha)$, the growth rate of the gravity wave and $\delta = \text{Im}(\alpha)$ is the frequency shift. The growth rate formula is decomposed of several independent terms

$$\lambda = \underbrace{\lambda_v}_{destab.} + \underbrace{\lambda_{vv} + \lambda_{hh}}_{quasi-static} + \underbrace{\lambda_{visc}}_{visc.\ damping} \tag{31}$$

The first term $\lambda_v \lesseqgtr 0$ is the potentially destabilizing term. It relates to the Lorentz-force interaction of the electrical current perturbation $\boldsymbol{j}_i$ caused by interface deformations with the background vertical magnetic field B_z (hence suffix $_v$). The terms $\lambda_{vv}, \lambda_{hh}$ are quasi-static MHD corrections. The term $\lambda_{vv} < 0$ is always negative and relates to magnetic damping caused by B_z. The term λ_{hh} related to the azimuthal field may be slightly positive, but is most often negative and always very small. These quasi-static effects are rarely modeled in metal pad roll theory since they are quadratic in magnetic field strength. The term $\lambda_{visc} < 0$ captures the viscous damping of gravity waves. For the frequency shift, we similarly split

$$\delta = \delta_h + \delta_{vh} + \delta_{visc} \tag{32}$$

The term δ_h relates to the Lorentz-force interaction of $\boldsymbol{j}_i$ caused by interface deformations with the background horizontal (azimuthal) magnetic field $B_\theta = \mu_0 Jr/2$ (hence suffix $_h$). In agreement with previous studies [3, 7] we find that this coupling cannot be destabilizing. The term δ_{vh} is a small quasi-static correction related to both B_θ and B_z. Finally, δ_{visc} is a frequency shift caused by viscosity. We now calculate all these different terms.

1. MPR instability in the magneto-static and inviscid limit : growth rate λ_v and frequency shift δ_h

In this section, we focus on the leading terms in the growth rate and frequency shift formulae, λ_v and δ_h. This may done in the inviscid limit $\nu_i = 0$ and assuming that $\sigma_i \omega RB/J \ll 1$ so that the magnetostatic approximation of Ohm's law $\boldsymbol{j}_i \approx -\sigma_i \boldsymbol{\nabla} \varphi_i$ may be used. Viscous and magnetic dissipation are outcasted in this entire section.

We propose the following Ansatz to the linear inviscid and magneto-static limit of the linearized problem defined in section II B :

$$[\boldsymbol{u}_i, p_i, \eta, \boldsymbol{j}_i, \varphi_i, \boldsymbol{b}_i] = \left(\left[\widehat{\boldsymbol{u}}_i, \widehat{p}_i, \widehat{\eta}, \widehat{\boldsymbol{j}}_i, \widehat{\varphi}_i, \widehat{\boldsymbol{b}}_i\right] + \left[\widetilde{\boldsymbol{u}}_i, \widetilde{p}_i, \widetilde{\eta}, \widetilde{\boldsymbol{j}}_i, \widetilde{\varphi}_i, \widetilde{\boldsymbol{b}}_i\right] \right) e^{i\omega t} \, e^{\alpha t} \tag{33}$$

In this notation, tilded variables are small perturbations with respect to the hatted variables, just as the complex shift α is small with respect to ω that will be frequency of the gravity waves. We inject this Ansatz into the governing equations and we treat the Lorentz force term perturbatively.

At leading order, we find the balance

$$\rho_i(i\omega)\widehat{\boldsymbol{u}}_i + \boldsymbol{\nabla}\widehat{p}_i = 0 \; , \; \boldsymbol{\nabla}\cdot\widehat{\boldsymbol{u}}_i = 0 \; , \; \widehat{\boldsymbol{j}}_i = -\sigma_i\boldsymbol{\nabla}\widehat{\varphi}_i \; , \; \boldsymbol{\nabla}\cdot\widehat{\boldsymbol{j}}_i = 0 \; , \; \boldsymbol{\nabla}\times\widehat{\boldsymbol{b}}_i = \mu_0\widehat{\boldsymbol{j}}_i \; , \; \boldsymbol{\nabla}\cdot\widehat{\boldsymbol{b}}_i = 0 \tag{34}$$

Notice that the Lorentz-force is absent in the momentum equation. Boundary conditions for the hatted fields can be copied from $(4 \to 8)$ and by replacing $\partial_t \to i\omega$. We need to solve this problem in order to specify all the first order quantities. The hydrodynamical fields $\widehat{\boldsymbol{u}}_i, \widehat{p}_i, \widehat{\eta}$ and the frequency ω were already given above. The electrical potential $\widehat{\varphi}_i$ is harmonic ($\boldsymbol{\nabla}^2\widehat{\varphi}_i = 0$) and related to the surface elevation $\widehat{\eta}$ by the jump condition (7b). We find it as

$$\begin{bmatrix} \widehat{\varphi}_1 \\ \widehat{\varphi}_2 \end{bmatrix} = \frac{JkA}{\omega} \frac{\sigma_1^{-1} - \sigma_2^{-1}}{\sigma_1^{-1}\tanh(kH_1) + \sigma_2^{-1}\tanh^{-1}(kH_2)} \begin{bmatrix} -i\sinh(k(z-H_1))/(\sigma_1\cosh(kH_1)) \\ -i\cosh(k(z+H_2))/(\sigma_2\sinh(kH_2)) \end{bmatrix} J_m(kr)\,e^{im\theta} \tag{35}$$

The isolating sidewall condition is automatically satisfied since $J'_m(kR) = 0$, by definition (see (12)) and electrical top and bottom boundary conditions too. Electrical currents $\widehat{\boldsymbol{j}}_i = -\sigma_i\boldsymbol{\nabla}\varphi_i$ are easily calculated from the previous potentials. The magnetic field perturbations $\widehat{\boldsymbol{b}}_i$ can be calculated in a (difficult) step by using for example the Biot-Savart law, but this will not be necessary here: $\widehat{\boldsymbol{b}}_i$ will not be explicitly required to evaluate the complex shift α. It is instructive to notice the systematic quadratures between the different leading order fields :

$$\frac{\{\widehat{\phi}_i \; , \; \widehat{u}_{i,r} \; , \; \widehat{u}_{i,z} \; , \; \widehat{j}_{i,\theta} \; , \; \widehat{b}_{i,r} \; , \; \widehat{b}_{i,z}\}}{A\exp(im\theta)} \in \mathbb{R} \quad , \quad \frac{\{\widehat{\eta}_i \; , \; \widehat{u}_{i,\theta} \; , \; \widehat{\varphi}_i \; , \; \widehat{j}_{i,r} \; , \; \widehat{j}_{i,z} \; , \; \widehat{b}_{i,\theta}\}}{A\exp(im\theta)} \in i\mathbb{R} \; , \tag{36}$$

As shown below, this information alone allows to understand why vertical magnetic fields are destabilizing and why horizontal magnetic fields can only induce a frequency shift in the perturbative limit.

All the leading order fields that are needed for the calculation of the shift α are now specified and so, we can write the next order in the perturbation problem. From the momentum and mass balance, we have

$$\alpha\rho_i\widehat{\boldsymbol{u}}_i + i\omega\rho_i\widetilde{\boldsymbol{u}}_i + \boldsymbol{\nabla}\widetilde{p}_i = \widehat{\boldsymbol{j}}_i \times \boldsymbol{B} + \boldsymbol{J} \times \widehat{\boldsymbol{b}}_i \tag{37a}$$

$$\boldsymbol{\nabla}\cdot\widetilde{\boldsymbol{u}}_i = 0 \tag{37b}$$

Note that the (small) Lorentz-force is now present in the right hand of the momentum balance and that it can be calculated using the first order fields $\widehat{\boldsymbol{j}}_i$ and $\widehat{\boldsymbol{b}}_i$. Equations for the corrections $\widetilde{\boldsymbol{j}}_i, \widetilde{\varphi}_i, \widetilde{\boldsymbol{b}}_i$ do not require consideration as they do not affect the eigenvalue shift α. The hydrodynamical boundary conditions for the tilded variables can be copied from (4) and (5) except for the kinematic boundary conditions that are different

$$\alpha\widehat{\eta} + i\omega\widetilde{\eta} = \widetilde{u}_{i,z}|_{z=0} \tag{38}$$

Next to $i\omega\widetilde{\eta}$, we find the term $\alpha\widehat{\eta}$ that is proportional to the small shift α. To find an equation for α, we express a solvability condition (also known as the Fredholm alternative). Here this condition corresponds to summing the combination $\int_{V_i}[\widehat{\boldsymbol{u}}_i^* \cdot \text{(37a)} + \widehat{p}_i^* \text{(37b)}]dV$ over both fluid regions $i = 1, 2$, which yields

$$\sum_{i=1,2}\int_{V_i} \left[\widehat{\boldsymbol{u}}_i^* \cdot (\alpha\rho_i\widehat{\boldsymbol{u}}_i + i\omega\rho_i\widetilde{\boldsymbol{u}}_i + \boldsymbol{\nabla}\widetilde{p}_i) + \widehat{p}_i^*\boldsymbol{\nabla}\cdot\widetilde{\boldsymbol{u}}_i\right]dV = \underbrace{\sum_{i=1,2}\int_{V_i} \widehat{\boldsymbol{u}}_i^* \cdot (\widehat{\boldsymbol{j}}_i \times \boldsymbol{B} + \boldsymbol{J} \times \widehat{\boldsymbol{b}}_i)\,dV}_{\mathcal{P}} \tag{39}$$

We introduce the notation $\mathcal{P}$ for the "power" injected by the Lorentz-force. In the left hand side, we can use partial integration to bring all spatial derivates back to the hatted variables. Using the leading order balances (34) and some basic vector calculus, we then find that this reduces to

$$\underbrace{\alpha \sum_{i=1}^{2} \int_{V_i} \rho_i |\widehat{\boldsymbol{u}}_i|^2 \mathrm{d}V}_{T_1} + \underbrace{\sum_{i=1}^{2} \oint_{\delta V_i} \left(\widehat{p}_i^* \widetilde{\boldsymbol{u}}_i + \widetilde{p}_i \widehat{\boldsymbol{u}}_i^*\right) \cdot \boldsymbol{n}_i \, \mathrm{d}S}_{T_2} = \mathcal{P} \tag{40}$$

The first group of terms T_1 is proportional to kinetic energy. Using the boundary conditions for the hatted and tilded variables, we can reduce the second group T_2 to

$$\begin{aligned} T_2 &= \alpha \int_{\mathcal{S}} \left(\widehat{p}_2^* - \widehat{p}_1^*\right)|_{z=0} \, \widehat{\eta} \, \mathrm{d}S \\ &= \alpha \int_{\mathcal{S}} \left(-\gamma_{1|2} \boldsymbol{\nabla}^2 \widehat{\eta}^* + (\rho_2 - \rho_1)g\widehat{\eta}^*\right) \, \widehat{\eta} \, \mathrm{d}S = \alpha \int_{\mathcal{S}} \left(\gamma_{1|2}|\boldsymbol{\nabla}\widehat{\eta}|^2 + (\rho_2 - \rho_1)g|\widehat{\eta}|^2\right)|_{z=0} \, \mathrm{d}S \\ &= \underbrace{\alpha \left[(\rho_2 - \rho_1)g + \gamma_{1|2}k^2\right] \int_{\mathcal{S}} |\widehat{\eta}|^2 \, \mathrm{d}S}_{\mathcal{K}} \end{aligned} \tag{41}$$

In writing the alternative to the second equation, we used the boundary condition $\partial_r \widehat{\eta}|_{r=R} = 0$, that is always satisfied by our inviscid gravity waves if the contact angle is 90^0. This also allows to see that T_2 is proportional to potential energy. The quantity $\mathcal{K} \in \mathbb{R}$ is a notation that will be used in what follows and it can be explicitly calculated using the expression for $\widehat{\eta}$ (see Appendix A). In summary, $T_1 + T_2$ is proportional to the mechanical energy. Using partial integration, the fact that waves derive from harmonic potentials and the hydrodynamic boundary conditions, one can further demonstrate that $T_1 = T_2$, for the simple harmonic wave under study :

$$\begin{aligned} T_1 &= \alpha \left[\rho_1 \oint_{\delta V_1} \widehat{\phi}_1^* \boldsymbol{\nabla}\widehat{\phi}_1 \cdot \boldsymbol{n}_1 \mathrm{d}S + \rho_2 \oint_{\delta V_2} \widehat{\phi}_2^* \boldsymbol{\nabla}\widehat{\phi}_2 \cdot \boldsymbol{n}_2 \mathrm{d}S\right] \\ &= \alpha \int_{\mathcal{S}} (-\mathrm{i}\rho_1 \omega \widehat{\phi}_1^* + \mathrm{i}\rho_2 \omega \widehat{\phi}_2^*)|_{z=0} \, \widehat{\eta} \, \mathrm{d}S \\ &= \alpha \int_{\mathcal{S}} (\widehat{p}_2^* - \widehat{p}_1^*)|_{z=0} \, \widehat{\eta} \, \mathrm{d}S = T_2 \end{aligned} \tag{42}$$

This has as consequence that the solvability condition (39) reduces to a mere $2\alpha\mathcal{K} = \mathcal{P}$ and the equation for the eigenvalue shift to $\alpha = \mathcal{P}/2\mathcal{K}$. We split $\mathcal{P} = \mathcal{P}_v + \mathcal{P}_h$ with

$$\mathcal{P}_v = \sum_{i=1,2} \int_{V_i} \widehat{\boldsymbol{u}}_i^* \cdot \left(\widehat{\boldsymbol{j}}_i \times B_z \boldsymbol{e}_z\right) \mathrm{d}V \quad , \quad \mathcal{P}_h = \sum_{i=1,2} \int_{V_i} \widehat{\boldsymbol{u}}_i^* \cdot \left[\widehat{\boldsymbol{j}}_i \times (\mu_0 Jr/2)\boldsymbol{e}_\theta + J\boldsymbol{e}_z \times \widehat{\boldsymbol{b}}_i\right] \mathrm{d}V \tag{43a}$$

to separate the contributions due to the vertical and the horizontal magnetic fields. In the formula for $\mathcal{P}_h$, the second term involves the magnetic field $\widehat{\boldsymbol{b}}_i$. Using the potential nature of the flow and $\boldsymbol{\nabla} \times (J\boldsymbol{e}_z) = \boldsymbol{0}$, we can rewrite

$$\begin{aligned} \widehat{\boldsymbol{u}}_i^* \cdot \left(J\boldsymbol{e}_z \times \widehat{\boldsymbol{b}}_i\right) &= \boldsymbol{\nabla}\widehat{\phi}_i^* \cdot \left(J\boldsymbol{e}_z \times \widehat{\boldsymbol{b}}_i\right) \\ &= \boldsymbol{\nabla} \cdot \left(\widehat{\phi}_i^* \left(J\boldsymbol{e}_z \times \widehat{\boldsymbol{b}}_i\right)\right) + \widehat{\phi}_i^* J\boldsymbol{e}_z \cdot (\boldsymbol{\nabla} \times \widehat{\boldsymbol{b}}_i) \end{aligned} \tag{44}$$

Using Ampère's law $\boldsymbol{\nabla} \times \widehat{\boldsymbol{b}}_i = \mu_0 \widehat{\boldsymbol{j}}_i$ and integrating over the volume then yields

$$\mathcal{P}_h = \sum_{i=1,2} \int_{V_i} \left\{\widehat{\boldsymbol{u}}_i^* \cdot \left[\widehat{\boldsymbol{j}}_i \times (\mu_0 Jr/2)\boldsymbol{e}_\theta\right] + \mu_0 J\widehat{\phi}_i^* \widehat{j}_{i,z}\right\} \mathrm{d}V + \underbrace{J \int \widehat{\phi}_i^* \left(\widehat{\boldsymbol{b}}_i \times \boldsymbol{n}_i\right) \cdot \boldsymbol{e}_z \, \mathrm{d}S}_{=0} \tag{45}$$

This allows to understand why the use of the simplifying magnetic boundary condition (8), indeed allows to calculate $\mathcal{P}_h$ without knowledge of $\widehat{\boldsymbol{b}}_i$. Both integrals $\mathcal{P}_v$ and $\mathcal{P}_h$ have been explicitly evaluated (see Appendix A). From the quadrature rules of (36) we can readily identify that $\mathcal{P}_v \in \mathbb{R}$ by symbolically calculating the real or imaginary character of the (mixed) products in the integranda, e.g.

$$\widehat{\boldsymbol{u}}_i^* \cdot (\widehat{\boldsymbol{j}}_i \times B_z \boldsymbol{e}_z) = \begin{vmatrix} \widehat{u}_{r,i}^* & \widehat{j}_{r,i} & 0 \\ \widehat{u}_{\theta,i}^* & \widehat{j}_{\theta,i} & 0 \\ \widehat{u}_{z,i}^* & \widehat{j}_{z,i} & B_z \end{vmatrix} \quad \longrightarrow \quad \begin{vmatrix} \mathbb{R} & \mathrm{i}\mathbb{R} & 0 \\ \mathrm{i}\mathbb{R} & \mathbb{R} & 0 \\ \mathbb{R} & \mathrm{i}\mathbb{R} & \mathbb{R} \end{vmatrix} \in \mathbb{R} \tag{46}$$

and similar for $\mathcal{P}_h \in i\mathbb{R}$. This implies that the eigenvalue shift α can be decomposed as

$$\alpha = \underbrace{\frac{\mathcal{P}_v}{2\mathcal{K}}}_{\lambda_v} + \underbrace{\frac{\mathcal{P}_h}{2\mathcal{K}}}_{i\delta_v} \tag{47}$$

According to our model and at this order of the expansion, only the vertical magnetic field component B_z can destabilize gravity waves that will grow at rates λ_v. The self-generated, horizontal magnetic field is not destabilizing but shifts the frequency of the wave by δ_h. This result is coherent with the analysis of [3, 7]. All formulae can be evaluated analytically and yield the explicit formula

$$\lambda_v = \frac{\omega}{2} \frac{JB_z}{(\rho_2 - \rho_1)g + \gamma_{1|2}k^2} \frac{m}{(kR)^2 - m^2} \left(\tanh(kH_1) + \frac{kH_2}{\sinh^2(kH_2)} + \frac{1}{\tanh(kH_2)} \right) \Lambda \tag{48a}$$

$$\delta_h = \frac{\omega}{4} \frac{\mu_0 J^2 k^{-1}}{(\rho_2 - \rho_1)g + \gamma_{1|2}k^2} \frac{(kR)^2 - 2m^2}{(kR)^2 - m^2} \left(\frac{kH_1}{\sinh(kH_1)\cosh(kH_1)} \right) \Lambda \tag{48b}$$

where

$$\Lambda = \frac{\sigma_1^{-1} - \sigma_2^{-1}}{\sigma_1^{-1}\tanh(kH_1) + \sigma_2^{-1}\tanh^{-1}(kH_2)} \tag{48c}$$

We have validated these formula by comparing them with numerical evaluations of the integrals of $\mathcal{P}_v, \mathcal{P}_h, \mathcal{K}$ computed using a simple quadrature rule on a two-dimensional $r - z$ grid. In both λ_v and δ_h, we see dimensionless factors that balance the typical strength of the Lorentz force (JB_z in λ_v, $\mu_0 J^2 k^{-1}$ in δ_h) with respect to gravitational and capillary restoring forces ($(\rho_2 - \rho_1)g + \gamma_{1|2}k^2$). We see that the growth rate $\lambda_v \sim m$, so axisymmetric waves with $m = 0$ can never be destabilized. The number Λ is a conductivity dependent factor that is not often seen in metal pad literature. It clearly shows that a jump in electrical conductivity $\sigma_1 \neq \sigma_2$ is essential for instability.

We can derive an inviscid instability criterion for the common case of $\sigma_1 \ll \sigma_2$. Since $(kR)^2 - m^2 > 0$ always (see Appendix A), inviscid instability or $\lambda_v > 0$ requires

$$\text{Sgn}(JB_z m\omega) > 0 \quad \Rightarrow \quad \text{wave is MPR-unstable} \tag{49}$$

In reduction cells, we further have $J < 0$ as the reduction current flows from top to bottom and if $B_z > 0$, this criterion learns us that only rotating waves with $m\omega < 1$ can be destabilized. This corresponds to waves that rotate in the positive or anti-clockwise direction when seen from above and coincides with what can be expected from the Sele-mechanism [2]. Note also that there is no threshold for the inviscid MPR-instability, also coherent with previous results [9, 10].

The general formula for the growth rate take simpler asymptotic forms in the limit of large conductivity jumps and for deep or shallow fluid layers. In the deep limit $kH_i \gg 1$ and with $\sigma_1/\sigma_2 \ll 1$ we find

$$\lambda_{v,deep} \approx \frac{JB_z}{(\rho_2 - \rho_1)g + \gamma_{1|2}k^2} \frac{m\omega_{deep}}{(kR)^2 - m^2} \tag{50a}$$

$$\delta_{h,deep} \approx 0 \tag{50b}$$

where

$$\omega_{deep} \approx \sqrt{\frac{(\rho_2 - \rho_1)gk + \gamma_{1|2}k^3}{\rho_1 + \rho_2}} \tag{51}$$

For shallow layers $kH_i \ll 1$ and with $\sigma_1/\sigma_2 \ll (kH_1)(kH_2)$ we have

$$\lambda_{v,shallow} \approx \frac{JB_z}{(\rho_2 - \rho_1)g + \gamma_{1|2}k^2} \frac{m\omega_{shallow}}{(kR)^2 - m^2} \frac{1}{(kH_1)(kH_2)} \tag{52a}$$

$$\delta_{h,shallow} \approx \frac{\omega_{shallow}}{4} \frac{\mu_0 J^2 k^{-1}}{(\rho_2 - \rho_1)g + \gamma_{1|2}k^2} \frac{(kR)^2 - 2m^2}{(kR)^2 - m^2} \frac{1}{kH_1} \tag{52b}$$

where

$$\omega_{shallow} \approx \sqrt{\frac{(\rho_2 - \rho_1)gk^2 + \gamma_{1|2}k^4}{\rho_1 H_1^{-1} + \rho_2 H_2^{-1}}} \tag{53}$$

The shallow approximation is commonly adopted in metal pad roll literature and for long-wavelength waves, surface tension usually is ignored. In that limit, we can rewrite the growth rate formula as

$$\lambda_{v,shallow} \approx \frac{JB_z}{\sqrt{(\rho_2 - \rho_1)g(\rho_1 H_1^{-1} + \rho_2 H_2^{-1})}} \frac{R}{H_1 H_2} \frac{m}{\kappa_{mn}(\kappa_{mn} - m^2)} \tag{54}$$

In this formula, we separated a wave-dependent factor that only depends on κ_{mn} and m, from a factor that groups all other physical and geometrical parameters. It allows to see that the growth rate increases proportionally to the lateral extend R of the shallow cell (if J is held fixed). Alternatively, we can also write

$$\lambda_{v,shallow} \approx \frac{m\omega_{shallow}}{\kappa_{mn}^2 - m^2} \frac{\beta}{\kappa_{mn}^2} \quad , \quad \beta = \frac{JB_z}{(\rho_2 - \rho_1)g} \frac{R^2}{H_1 H_2} \tag{55}$$

The shallow-limit growth rate is proportional to the non-dimensional group β, that appeared in many previous studies on metal pad roll instability. In Appendix B, we develop further on this small gap limit and show that the growth rate formula (55) is compatible with existing shallow layer models of [9, 10] in the double limit of asymptotically small $kH_i \ll 1$ and $\beta \ll 1$.

In Appendix C, we explore the effect of symmetric top and bottom boundary conditions (fixed potential or fixed normal current) on the metal pad roll instability, also studied in [44]. The mixed electrical boundary conditions we used here in the body of the article (fixed potential on top, fixed normal current on the bottom), always yield much more unstable cells in the shallow limit. In deep cells, the precise choice for the electrical top and bottom boundary conditions has no influence.

2. *Quasi-static corrections : damping λ_{vv} & λ_{hh}, frequency shift δ_{vh}*

When the magnetic field strength $B = \mu_0 JR$ or B_z is too high, the simplifying assumption $\sigma_i \omega RB/J \ll 1$ is no longer satisfied. In that case, the quasi-static approximation of MHD is required to include how fluid flows can modify the electrical current density through induction. We need to use

$$\boldsymbol{j}_i = \sigma_i(-\boldsymbol{\nabla}\varphi_i + \boldsymbol{u}_i \times \boldsymbol{B}) \tag{56}$$

in replacement of the static approximation $\boldsymbol{j}_i \approx -\sigma_i\boldsymbol{\nabla}\varphi_i$ of the previous section, at least in the Aluminum layer where $\sigma_2 \gg \sigma_1$. Next to the terms λ_v and δ_h this will yield quasi-static corrections $\lambda_{vv} \sim B_z^2$, $\lambda_{hh} \sim B_\theta^2$ and $\delta_{vh} \sim B_\theta B_z$ to the growth rate and frequency shift.

If the quasi-static version of Ohm's law is to be used, we need to extend the perturbation Ansatz (33) to

$$[\boldsymbol{u}_i, p_i, \eta, \boldsymbol{j}_i, \varphi_i] = \left(\left[\widehat{\boldsymbol{u}}_i, \widehat{p}_i, \widehat{\eta}, \widehat{\boldsymbol{j}}_i + \widehat{\boldsymbol{\mathcal{J}}}_i^v + \widehat{\boldsymbol{\mathcal{J}}}_i^h, \widehat{\varphi}_i + \widehat{\Psi}_i^v + \widehat{\Psi}_i^h, \widehat{\boldsymbol{b}}_i + \widehat{\boldsymbol{\mathcal{B}}}_i^v + \widehat{\boldsymbol{\mathcal{B}}}_i^h\right] + \left[\widetilde{\boldsymbol{u}}_i, \widetilde{p}_i, \widetilde{\eta}, \widetilde{\boldsymbol{j}}_i, \widetilde{\varphi}_i, \widetilde{\boldsymbol{b}}_i\right]\right) e^{i\omega t} e^{\alpha t} \tag{57}$$

Fields $\widehat{\boldsymbol{u}}_i, \widehat{p}_i, \widehat{\eta}, \widehat{\varphi}_i, \widehat{\boldsymbol{j}}_i, \widehat{\boldsymbol{b}}_i$ are identical to those of the previous section and capture all magneto-hydrodynamical effects related to surface elevation considered before. Quasi-static corrections for the electrical potential and the current densities relate to either the vertical magnetic (superscripts ^{v}) or horizontal magnetic field (superscript ^{h}). We define the current density corrections as

$$\widehat{\boldsymbol{\mathcal{J}}}_i^v = \sigma_i(-\boldsymbol{\nabla}\widehat{\Psi}_i^v + \widehat{\boldsymbol{u}}_i \times B_z \boldsymbol{e}_z) \quad , \quad \widehat{\boldsymbol{\mathcal{J}}}_i^h = \sigma_i(-\boldsymbol{\nabla}\widehat{\Psi}_i^h + \widehat{\boldsymbol{u}}_i \times (\mu_0 Jr/2)\boldsymbol{e}_\theta) \tag{58}$$

and they need to satisfy $\boldsymbol{\nabla} \cdot \widehat{\boldsymbol{\mathcal{J}}}_i^v = \boldsymbol{\nabla} \cdot \widehat{\boldsymbol{\mathcal{J}}}_i^h = 0$. In terms of the electrical potentials, this defines Laplace and Poisson problems

$$\boldsymbol{\nabla}^2\widehat{\Psi}_i^v = 0 \quad , \quad \boldsymbol{\nabla}^2\widehat{\Psi}_i^h = -\mu_0 J\widehat{u}_{z,i} \tag{59}$$

that need to be solved together with inhomogeneous boundary conditions:

$$\widehat{\Psi}_1^v|_{z=H_1} = 0 \quad , \quad \widehat{\Psi}_1^h|_{z=H_1} = 0 \tag{60a}$$

$$\partial_z\widehat{\Psi}_2^v|_{z=-H_2} = 0 \quad , \quad \partial_z\widehat{\Psi}_2^h|_{z=-H_2} = (\mu_0 Jr/2)\widehat{u}_{2,r}|_{z=-H_2} \tag{60b}$$

$$\partial_r\widehat{\Psi}_i^v|_{r=R} = B_z\widehat{u}_{i,\theta}|_{r=R} \quad , \quad \partial_r\widehat{\Psi}_i^h|_{r=R} = -(\mu_0 JR/2)\widehat{u}_{i,z}|_{r=R} \tag{60c}$$

$$\widehat{\Psi}_1^v|_{z=0} = \widehat{\Psi}_2^v|_{z=0} \quad , \quad \widehat{\Psi}_1^h|_{z=0} = \widehat{\Psi}_2^h|_{z=0} \tag{60d}$$

$$\sigma_1\partial_z\widehat{\Psi}_1^v|_{z=0} = \sigma_2\partial_z\widehat{\Psi}_2^v|_{z=0} \quad , \quad \sigma_1\left(-\partial_z\widehat{\Psi}_1^h + (\mu_0 Jr/2)\widehat{u}_{1,r}\right)_{z=0} = \sigma_2\left(-\partial_z\widehat{\Psi}_2^h + (\mu_0 Jr/2)\widehat{u}_{2,r}\right)_{z=0} \tag{60e}$$

These problems have no simple analytical solution but we can find $\widehat{\Psi}_i^v$ and $\widehat{\Psi}_i^h$ numerically. The field profiles are Fourier expanded along θ: $\widehat{\Psi}_i^v = f_i^v(r,z)\exp(im\theta)$, $\widehat{\Psi}_i^h = f_i^h(r,z)\exp(im\theta)$ and the remaining two-dimensional problem for f_i^v and f_i^h is solved using a standard second order finite difference method on a uniform grid with $2 \times (M+1)^2$ points:

$$\begin{cases} \text{region 1}: & (i\delta r, j\delta z_1) \\ \text{region 2}: & (i\delta r, -j\delta z_2) \end{cases} , \quad \forall i,j \in \{0,1,\ldots,M\}$$

Here $\delta r = R/M$, $\delta z_1 = H_1/M$, $\delta z_2 = H_2/M$. Radial and vertical derivatives appearing in the boundary conditions are discretised using second order decentered finite difference formula. At the axis, we use the regularity condition $\widehat{\Psi}_i^v|_{r=0} = \widehat{\Psi}_i^h|_{r=0} = 0$ for $m \neq 0$. The numerical code itself is provided as supplementary material.

As in the previous section, we do not need to calculate the quasistatic magnetic field corrections $\widehat{\mathcal{B}}_i^v$ and $\widehat{\mathcal{B}}_i^h$ provided that they satisfy the boundary condition (8). We can deduce the following rules of quadrature

$$\frac{\{\widehat{\psi}_i^h \,,\, \widehat{\mathcal{J}}_{i,r}^h \,,\, \widehat{\mathcal{J}}_{i,z}^h \,,\, \widehat{\mathcal{J}}_{i,\theta}^v \,,\, \widehat{\mathcal{B}}_{i,r}^v \,,\, \widehat{\mathcal{B}}_{i,z}^v \,,\, \widehat{\mathcal{B}}_{i,\theta}^h\}}{A\exp(im\theta)} \in \mathbb{R} \quad,\quad \frac{\{\widehat{\psi}_i^v \,,\, \widehat{\mathcal{J}}_{i,r}^v \,,\, \widehat{\mathcal{J}}_{i,z}^v \,,\, \widehat{\mathcal{J}}_{i,\theta}^h \,,\, \widehat{\mathcal{B}}_{i,r}^h \,,\, \widehat{\mathcal{B}}_{i,z}^h \,,\, \widehat{\mathcal{B}}_{i,\theta}^v\}}{A\exp(im\theta)} \in i\mathbb{R} \,, \qquad (61)$$

Supposing that the quasi-static field corrections are known, we recalculate the complex eigenvalue shift α by writing a modified solvability condition. This leads here to

$$2\alpha\mathcal{K} = \mathcal{P} + \underbrace{\sum_{i=1,2} \int_{V_i} \widehat{\boldsymbol{u}}_i^* \cdot \left[\left(\widehat{\boldsymbol{\mathcal{J}}}_i^v + \widehat{\boldsymbol{\mathcal{J}}}_i^h\right) \times \boldsymbol{B} + \boldsymbol{J} \times \left(\widehat{\boldsymbol{\mathcal{B}}}_i^v + \widehat{\boldsymbol{\mathcal{B}}}_i^h\right)\right]\mathrm{d}V}_{\mathcal{Q}} \qquad (62)$$

The quantities $\mathcal{K}$ and $\mathcal{P}$ are as before. The new term $\mathcal{Q}$ isolates the effect of the quasistatic field corrections. We split it in three parts

$$\mathcal{Q} = \mathcal{Q}_{vv} + \mathcal{Q}_{hh} + \mathcal{Q}_{vh} \qquad (63)$$

with

$$\mathcal{Q}_{vv} = \sum_{i=1,2} \int_{V_i} \widehat{\boldsymbol{u}}_i^* \cdot \left(\widehat{\boldsymbol{\mathcal{J}}}_i^v \times B_z \boldsymbol{e}_z\right)\mathrm{d}V$$

$$\mathcal{Q}_{hh} = \sum_{i=1,2} \int_{V_i} \widehat{\boldsymbol{u}}_i^* \cdot \left(\widehat{\boldsymbol{\mathcal{J}}}_i^h \times (\mu_0 Jr/2)\boldsymbol{e}_\theta + \boldsymbol{J} \times \widehat{\boldsymbol{\mathcal{B}}}_i^h\right)\mathrm{d}V$$

$$\mathcal{Q}_{vh} = \sum_{i=1,2} \int_{V_i} \widehat{\boldsymbol{u}}_i^* \cdot \left(\widehat{\boldsymbol{\mathcal{J}}}_i^h \times B_z \boldsymbol{e}_z + \widehat{\boldsymbol{\mathcal{J}}}_i^v \times (\mu_0 Jr/2)\boldsymbol{e}_\theta + \boldsymbol{J} \times \widehat{\boldsymbol{\mathcal{B}}}_i^v\right)\mathrm{d}V \qquad (64)$$

Analyzing the integrals using the quadrature rules of (61), we readily deduce that $\mathcal{Q}_{vv}, \mathcal{Q}_{hh} \in \mathbb{R}$ whereas $\mathcal{Q}_{vh} \in i\mathbb{R}$. With $\alpha = \lambda + i\delta$ we have modified formulae for the growth rate λ and frequency shift δ

$$\lambda = \lambda_v + \underbrace{\frac{\mathcal{Q}_{vv}}{2\mathcal{K}}}_{\lambda_{vv}} + \underbrace{\frac{\mathcal{Q}_{hh}}{2\mathcal{K}}}_{\lambda_{hh}} \quad,\quad \delta = \delta_h + \underbrace{\mathrm{Im}\left(\frac{\mathcal{Q}_{vh}}{2\mathcal{K}}\right)}_{\delta_{vh}} \qquad (65)$$

In practice, the integrals in $\mathcal{Q}_{vv}$, $\mathcal{Q}_{hh}$, $\mathcal{Q}_{vh}$ are calculated numerically using the field profiles provided by the finite difference code. We use a simple trapezoidal quadrature rule to calculate the two-dimensional integral over (r,z).

The need to use a numerical approach to find the quasi-static corrections is slightly unsatisfying. Given the fact that $\sigma_1 \ll \sigma_2$, induction in the top electrolyte layer is very weak and we can approximate

$$\widehat{\boldsymbol{\mathcal{J}}}_1^v \approx \widehat{\boldsymbol{\mathcal{J}}}_1^h \approx \boldsymbol{0} \qquad (66)$$

in the electrolyte. We then need to solve (59), only in the Aluminium layer, together with boundary conditions (60b), (60c) and with (60e) replaced by

$$\partial_z \widehat{\Psi}_2^v|_{z=0} \approx 0 \quad,\quad \partial_z \widehat{\Psi}_2^h|_{z=0} \approx (\mu_0 Jr/2)\widehat{u}_{2,r}|_{z=0} \qquad (67)$$

Analytical solutions can be presented in terms of infinite series of harmonic functions. The calculation is quite laborious for $\widehat{\Psi}_2^h$ and is not presented here. For $\widehat{\Psi}_2^v$, it is more amenable and we have

$$\widehat{\Psi}_2^v = \left[C_0 \left(\frac{r}{R} \right)^m + \sum_{j=1}^{+\infty} C_j I_m(j\pi r/H_2) \cos(j\pi z/H_2) \right] e^{\mathrm{i}m\theta} \tag{68}$$

Here I_m is a modified Bessel function and $C_0, C_1, C_2, \ldots$ expansion coefficients. These coefficients are calculated by expressing the inhomogeneous boundary condition $\partial_r \widehat{\Psi}_2^v|_{r=R} = \widehat{u}_{\theta,2}|_{r=R} B_z$ that is projected onto the set of basis functions $\{\cos(j\pi z/H_2) \ , \ j \in \mathbb{N}\}$ using the orthogonality relation

$$\int_{-H_2}^0 \cos \frac{j\pi z}{H_2} \cos \frac{j'\pi z}{H_2} = \delta_{j,j'} \left\{ \begin{array}{ll} H_2 \ , & j = 0 \\ H_2/2 \ , & j \neq 0 \end{array} \right. \tag{69}$$

This yields

$$C_0 = -\mathrm{i} \frac{AB_z}{kH_2} J_m(kR) \ , \ \ C_j = -\mathrm{i} \frac{AB_z}{j\pi} \frac{4mJ_m(kR)}{(kR)(I_{m+1}(j\pi R/H_2) + I_{m-1}(j\pi R/H_2))} \frac{k^2}{k^2 + (j\pi/H_2)^2} \sinh(kH_2) \tag{70}$$

With this information we can calculate the integral $\mathcal{Q}_{vv}$, best rewritten as

$$\mathcal{Q}_{vv} \approx -\sigma_2 \int_{V_2} ||\widehat{\boldsymbol{u}}_i^* \times B_z \boldsymbol{e}_z||^2 \mathrm{d}V + \int_{V_2} \widehat{\boldsymbol{u}}_i^* \cdot \left(-\sigma_2 \boldsymbol{\nabla} \widehat{\Psi}_2^v \times B_z \boldsymbol{e}_z \right) \mathrm{d}V \tag{71}$$

This yields $\lambda_{vv} \approx \mathcal{Q}_{vv}/2\mathcal{K}$:

$$\lambda_{vv} \approx \frac{\sigma_2 B_z^2}{\dfrac{\rho_1}{\tanh(kH_1)} + \dfrac{\rho_2}{\tanh(kH_2)}} \left\{ -\frac{1}{4} \left(\frac{1}{\tanh(kH_2)} + \frac{kH_2}{\sinh^2(kH_2)} \right) \right.$$
$$\left. + \left(\frac{1}{k^2 R^2 - m^2} \right) \left[\frac{m}{kH_2} + 4m^2 \sum_{j=1}^{+\infty} \left(\frac{1}{j\pi} \right) \frac{k^3}{R(k^2 + (j\pi/H_2)^2)^2)} \frac{I_m(j\pi R/H_2)}{I_{m+1}(j\pi R/H_2) + I_{m-1}(j\pi R/H_2)} \right] \right\} \tag{72}$$

The first term in the curly brackets is negative and relates to the magnetic damping rate that we would have in containers with perfectly conducting walls (where $\widehat{\Psi}_2^v = 0$). The collection of terms on the second line is positive and it captures how the use of electrically insulating radial boundaries can render the magnetic damping less efficient. This physical observation is coherent with [42]. In practice, we observe a fast exponential decay of the terms in the sum over j, thus the faster as the cell is shallow. All following calculations are done by truncating the sum over j to the first 50 terms and we have checked the validity of this formula by comparing it with the result from the finite difference code (demonstrated below).

We can expand the previous formula for the magnetic damping rate in the shallow limit, $kH_i \ll 1$ and we find

$$\lambda_{vv,shallow} \approx \frac{\sigma_2 B_z^2}{\rho_1 \left(\dfrac{H_2}{H_1} \right) + \rho_2} \left(-\frac{1}{2} + \frac{m}{k^2 R^2 - m^2} \right) \tag{73}$$

All terms in the sum over j do not contribute significantly. Only the z-independent part of the potential $C_0(r/R)^m \exp \mathrm{i}m\theta$ has a significant weight. In the deep limit $kH_i \gg 1$, no simplified formula can be derived from (72), because too many terms remain significant in the sum over j. This is due to the fact that the cosinusoïdal basis used in the expansion is not adapted to the deep limit. It is possible to derive deep limit formula using Fourier transform methods.

3. Viscous corrections : damping λ_{visc}, frequency shift δ_{visc}

We finally also include the viscous effects in the perturbative calculation. Leading order viscous effects can be modeled as if the cell was in a purely hydrodynamical state $J = B_z = 0$, which then is a rather classical problem. Early work goes back to [45] who calculated viscous damping of waves in cylinders with only one fluid ($\rho_1 = 0$). The theory was successfully compared to experimental measurements in well polished cylinders, but not in brimful cylinders and not with all liquids. Viscous damping of gravity waves may significantly depend on the complex contact

line dynamics and on surface contamination (see discussions in e.g. [45, 46]) making the theoretical calculation of surface wave damping rates much more delicate than initially suspected.

Viscous damping rate formulas for waves in cylinders filled with two layers of fluid are not immediately available and they are calculated here. We ignore surface contamination effects and also the damping that is associated by what happens in the contact line region, too complex to model correctly. In the appendix D, we provide all details of our calculation. The method that we use is different from that of [45], but more closely relates to the asymptotic framework we have been using in the previous sections. In a nutshell, we further extend the asymptotic Ansatz (57) to

$$[\boldsymbol{u}_i + \overline{\boldsymbol{u}}_i, p_i + \overline{p}_i, \ldots] = \left(\left[\widehat{\boldsymbol{u}}_i + \widehat{\overline{\boldsymbol{u}}}_i, \widehat{p}_i + \widehat{\overline{p}}_i, \ldots \right] + \left[\widetilde{\boldsymbol{u}}_i + \widetilde{\overline{\boldsymbol{u}}}_i, \widetilde{p}_i + \widetilde{\overline{p}}_i, \ldots \right] \right) e^{(i\omega + \alpha)t} \tag{74}$$

for the flow and pressure variables. The fields $\widehat{\boldsymbol{u}}_i, \widehat{p}_i$ are the inviscid gravity wave profiles. Barred variables designate boundary layer corrections that only exist in $O(\sqrt{\nu_i/\omega})$ wide layers near the rigid walls. We calculate these viscous boundary layers, ignoring the specificity of the contact line region and ignoring contributions from the free interface that often are much weaker. Mass conservation in the viscous boundary layer causes a wall-normal pumping flow that enters our model through modifications in the solvability condition (39), via boundary terms. After having discarded unphysical terms that relate to the bad modeling of the contact line region, we find

$$\lambda_{visc} = -\frac{1}{\sqrt{2}} \sum_{i=1,2} \left\{ \frac{\sqrt{\frac{\nu_i |\omega|}{R^2}} \rho_i \left[k(R - H_i) \sinh^{-2}(kH_i) + \left(\frac{k^2 R^2 + m^2}{k^2 R^2 - m^2} \right) \tanh^{-1}(kH_i) \right]}{\left[\rho_1 \tanh^{-1}(kH_1) + \rho_2 \tanh^{-1}(kH_2) \right]} \right\} \tag{75}$$

and we also show that viscosity induces a small frequency shift

$$\delta_{visc} = \text{Sgn}(\omega) \, \lambda_{visc} \tag{76}$$

This shift always lowers the absolute value of the frequency of the wave. In appendix D, we further show that the damping rate λ_{visc} is identical to what results from the energy equation method used by [45], which gives us extra confidence about the formula.

In the shallow limit $kH_i \ll 1$, damping on bottom and top boundaries dominates and we can derive the asymptotic form

$$\lambda_{visc,shallow} \approx -\frac{1}{\sqrt{2}} \frac{\rho_1 H_1^{-2} \sqrt{\nu_1} + \rho_2 H_2^{-2} \sqrt{\nu_2}}{\rho_1 H_1^{-1} + \rho_2 H_2^{-1}} \sqrt{|\omega_{shallow}|} \tag{77}$$

In the deep limit, $kH_i \gg 1$, damping on the radial wall dominates and we can use

$$\lambda_{visc,deep} \approx -\frac{1}{\sqrt{2}} \left(\frac{k^2 R^2 + m^2}{k^2 R^2 - m^2} \right) \frac{1}{R} \frac{\rho_1 \sqrt{\nu_1} + \rho_2 \sqrt{\nu_2}}{\rho_1 + \rho_2} \sqrt{|\omega_{deep}|} \tag{78}$$

as asymptotically valid formula.

G. Applicability of the perturbative model: necessary conditions

We have provided sufficient conditions to apply the perturbation method, but necessary conditions can be derived a posteriori by expressing that

$$\left| \frac{\lambda_v}{\omega} \right| \ll 1 \quad , \quad \left| \frac{\lambda_{vv}}{\omega} \right| \ll 1 \quad , \quad \left| \frac{\lambda_{hh}}{\omega} \right| \ll 1 \quad , \quad \left| \frac{\lambda_{visc}}{\omega} \right| \ll 1 \quad , \quad \left| \frac{\delta_h}{\omega} \right| \ll 1 \quad , \quad \left| \frac{\delta_{vh}}{\omega} \right| \ll 1 \tag{79}$$

When these conditions are not verified, the theoretical formula become unsure or even wrong. This needs to be kept in mind before applying the theoretical formula.

III. EXPERIMENTAL STUDY OF VISCOUS DAMPING RATES

In [38], a detailed experimental study on orbital sloshing of waves in two and three fluid layer systems has been performed. In this configuration, the cylinder is horizontally translated along a circular path, which mainly drives

a large scale rotating wave $(m, n) = (1, 1)$, also the wave that is most frequently associated with the metal pad roll instability. By putting the orbital shaker suddenly to a stop, one can measure the viscous decay of this rotating gravity wave and compare this to the theoretical formula (75) for the viscous damping rate λ_{visc}.

The experimental set-up is shown in figure 2 (a): cylindrical containers of different aspect ratios were made from polished acrylic glass. For the present study we employed containers with dimensions $R = 5\,\text{cm}$ and total height $H_1 + H_2 = 10\,\text{cm}$ varying $H_2 = 0.15\,\text{cm}$ to $H_2 = 0.85\,\text{cm}$ in steps of $0.05\,\text{cm}$. Both top and bottom caps of the cylinder contain ten supply holes to attach up to ten ultrasound probes circulatory distributed around the central point with a distance of $42\,\text{mm}$. A small $5\,\text{mm}$ thick layer of acrylic glass was kept between the probes and the observation volume ensuring non-invasive ultrasound measurements of interfacial motion. The upper cap additionally contains a small filling hole of $4\,\text{mm}$ diameter enabling to degas the cell and to effortlessly adjust the position of the interface. The entire sample is placed on a sample holder, which facilitates ultrasound measurements also from below. This way, up to 20 ultrasound probes can be simultaneously employed making it possible to precisely reconstruct wave modes. The Ultrasound Doppler Velocimeter DOP 3010 from Signal-Processing was employed to drive up to ten ultrasound probes which produce beeps and listen for echoes. By directly identifying and tracking the ultrasound echo reflected at the interface, the interfacial wave motion can be precisely measured for amplitudes in the range $0.15\,\text{mm} \lesssim A \lesssim 10\,\text{mm}$. This novel acoustic measurement method can be also applied in opaque liquid metals. Finally, the sample holder is mounted onto a Kuhner LS-X lab-shaking table $(420 \times 420\,\text{mm})$, which can prescribe an ideal circular translation

$$\boldsymbol{r}_{orbital}(t) = \frac{d_s}{2}(\cos \Omega t \boldsymbol{e}_x + \sin \Omega t \boldsymbol{e}_y) \tag{80}$$

to the container with constant frequency Ω and shaking diameter d_s. The shaker was modified to allow for a continuous adjustment of the shaking diameter up to $d_s = 70\,\text{mm}$ and to set shaking frequencies from $\Omega = 20\,\text{rpm}$ up to $\Omega = 500\,\text{rpm}$ in steps of $1\,\text{rpm}$.

Different working liquids were tested in [38] in order to realize long-time stable interfaces in two- and three-layer systems with distinct wave properties and boundary conditions. For the present study we specially tailored a fluid combination. A top layer of Paraffinum Perliquidum ($\rho_1 = 0.846\,\text{g/cm}^3$, $\nu_1 = 36\,\text{mm}^2/\text{s}$, $\gamma_1 \approx 30\,\text{mN/m}$) with a bottom layer of Wacker® silicone oil AK 35 ($\rho_2 = 0.955\,\text{g/cm}^3$, $\nu_2 = 35\,\text{mm}^2/\text{s}$, $\gamma_2 = 20.7\,\text{mN/m}$) is getting very close to the idealized boundary condition supposed in this study. A meniscus was not visible and we observed an almost free-sliding contact line.

To measure the experimental damping rates we followed a strict protocol. Pre-measurements were conducted to find the eigenfrequency Ω of the mode $(m, n) = (1, 1)$ for each choice of H_2, since it is known from [47], that at resonance the forced wave motion is most similar to free gravity waves. We then drive the rotating wave at the resonant frequency, adjusting the shaking diameter d_s in order to drive waves that on the one hand are large enough to allow damping rate measurements, and on the other hand small enough to remain in the linear, non-breaking wave regime (amplitudes between $3\,\text{mm}$ and $5\,\text{mm}$ in practice). After the wave is settled in a saturated state, we turn off the shaking table. Subsequently, we give the wave some time (about one up to two periods) to transform into a "free" gravity wave. Then we determined the exponential decay rate $-\lambda$ by fitting the ansatz

$$A(t) = A_0 e^{\lambda t} \cos(\Omega t - \delta) \tag{81}$$

to the measured wave-amplitude. Here A_0 denotes the initial wave amplitude that also needs to fitted and introduces some uncertainty. In figure 2 (b) we compare the measured damping rates to the theoretical formula. Error bars were estimated by using different fitting time intervals. The measured decay rates are in very good agreement with the theoretical viscous damping rate. The theory slightly underestimates the measured damping rates. Figure 2 (b) also shows the theoretical damping rates in the shallow and deep water limits. The points of contact demonstrate that we have compared the damping rates in the full transitional regime between these simplified asymptotic limits that are more frequently analyzed in the literature.

The full experimental study of orbital sloshing of two and three-layer fluid systems will be presented in a separate article [38]. Here we can conclude that our perturbation theory can suitably predict the viscous damping rates of gravity waves of two-layer systems if the simplified boundary conditions at the contact line are fulfilled.

IV. APPLICATION TO SMALL AND LARGE REDUCTION CELLS

We now return back to the metal pad roll problem and apply our theory to two different reduction cells, a small one and a large one. To better see the strong geometrical difference between both cells, we show a sideview of both cells in figure 3, together with our parameter choices. We use realistic values of σ_i, ρ_i, ν_i. Surface tension will be either absent $\gamma_{1|2} = 0$ or equal to $\gamma_{1|2} = 0.5\,\text{N/m}$ [22] and $g = 9.81 m/s^2$, $\mu_0 = 4\pi\,10^{-7}$.
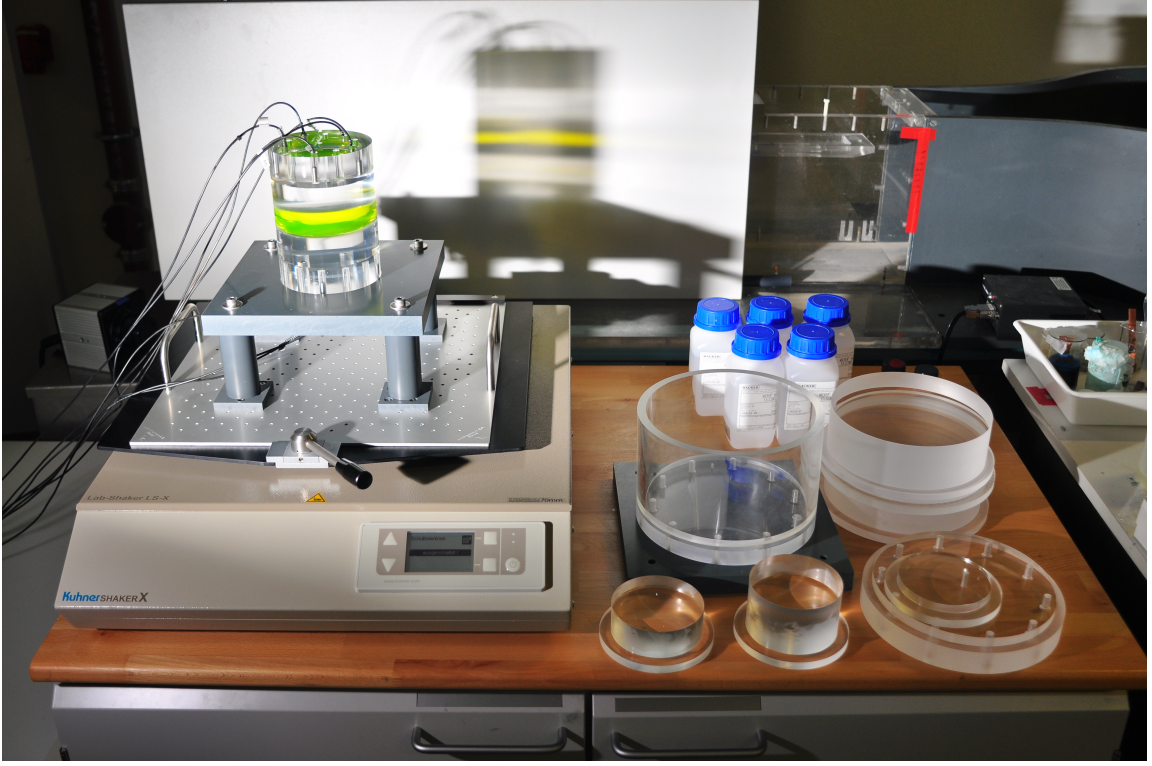
(a) experimental set-up used to measure viscous wave damping
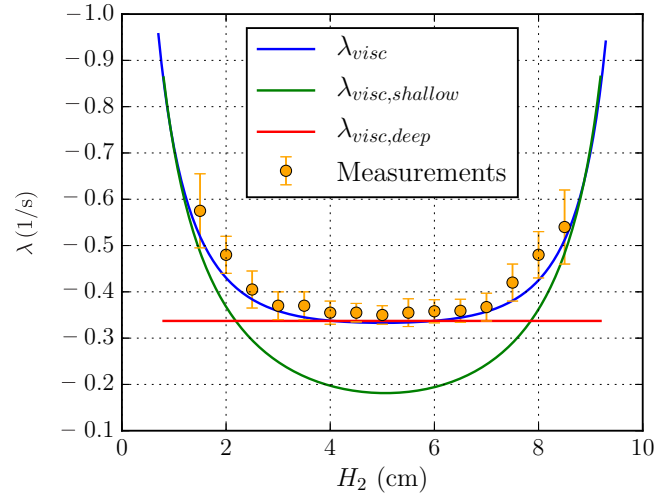
(b) measured and theoretical viscous damping rates

FIG. 2. (a) Photograph of the experimental set-up showing the cylindrical observation sample mounted on a Kuhner LS-X lab-shaker and different further individual parts to compose samples of various aspect ratios. In this picture, the cylinder was filled with silicon oil (top), water (middle) and paraffin oil (bottom) to realize a stable three-layer system and the water layer was colored to increase the visibility. (b) measured damping rates λ in comparison with the theoretical viscous damping rate due to equation (75) for different interfacial heights H_2. The theoretical damping rate is also shown within the shallow (77) and deep (78) water limits.

cell	R	H_1	H_2	ρ_1	ρ_2	σ_1	σ_2	ν_1	ν_2	$-J$	B_z
(a)	0.035	0.075	0.075	2150	2300	250	$3.5\,10^6$	$1.2\,10^{-6}$	$5.2\,10^{-7}$	$\leq 2 \times 10^4$	≤ 0.1
(b)	$0.5 \to 2.5$	0.05	0.30	"	"	"	"	"	"	1.5×10^4	0.001

FIG. 3. Physical parameters and sideview of the set-up for two configurations studied in the article. Values of R, H_i in m, ρ_i in $\mathrm{kg\,m^{-3}}$, σ_i in $\mathrm{S\,m^{-1}}$, ν_i in $\mathrm{m^2\,s^{-1}}$, J in $\mathrm{A\,m^{-2}}$, B_z in T. Configuration (a) is a small experimental cell inspired by the cylindrical cell studied in [22, 23]. Configuration (b) is a big cell with realistic heights of fluids and a large lateral extent (in this plot $R = 1\,\mathrm{m}$). The sideview was scaled to clearly see the difference in geometry

A. Small, laboratory scale cell

The small cell has radius $R = 0.035\,\mathrm{m}$ and $H_i = 0.075\,\mathrm{m}$. It bares little ressemblance with the large and shallow industrial Hall-Heroult cells but it is representative of a laboratory scale device such as that discussed in [22, 23] or in the experiments of [39, 40]. Small cells can only be destabilized with high enough J or B_z. We decide to keep J within realistic levels and for B_z we take the liberty to impose very high magnetic fields B_z, similar to what was done in [39, 40] and [22, 23].

1. Theoretical results

In Table I we provide numerical values for wavenumbers k and frequencies ω of several waves (m, n) together with all the different terms $\lambda_v, \lambda_{vv}, \lambda_{hh}, \lambda_{visc}$ that may affect the growth rate and δ_h, δ_{vh} that contribute to the frequency shift. Most data is presented relative to J, JB_z, J^2 in order to allow for more general use. Data for axisymmetric waves with $m = 0$ is not reported since they can never become unstable according to our theory. Focussing on λ_v/JB_z, we see the large scale sloshing mode $(m, n) = (1, 1)$ is not the only unstable wave. Without surface tension, the higher m modes are even more unstable, with surface tension, not. Waves with smaller radial structures, with $n \geq 2$ are always much less destabilized. The relative frequency shift δ_h/J^2 is always extremely low. The notation $\to 0$ suggests here values lower than 10^{-19}. This smallness is only partly due to the μ_0-factor in the formula. The quasi-static static corrections $\lambda_{vv}/B_z^2, \lambda_{hh}/J^2, \delta_{vh}/JB_z$ are independent of surface tension. The magnetic damping due to the vertical magnetic field λ_{vv}/B_z^2 increases with m and n. For λ_{hh}/J^2 we also find very small values. Here this mainly due to a μ_0^2 factor and we have checked that there are no problems with numerical precision. Remarkable is the fact that $\lambda_{hh}/J^2 > 0$ for the fundamental wave $(1, 1)$, so that this mode could in principle be very weakly destabilized without B_z provided that J would become unrealistically high. For the quasi-static frequency correction δ_{vh}/JB_z values are low and there is no clearly observable trend. In the last column, we see that the viscous dissipation of the waves increases with m. Surface tension increases the viscous dissipation, mainly because the frequency of the waves increases drastically.

From the previous table, it is clear that all horizontal field effects will be negligible when $J \sim 10^4\,\mathrm{A\,m^{-2}}$. In the small cell geometry, we can therefore approximate the growth rate and frequency shift as

$$\lambda \approx \lambda_v + \lambda_{vv} + \lambda_{visc} \quad , \quad \delta \approx \delta_{visc} \tag{82}$$

In figure 4, we show lines of marginal instability in the $J - B_z$ plane calculated using this data, for cases with and without surface tension. The first wave to be destabilized is the large scale sloshing wave with $(m, n) = (1, 1)$ followed by the other waves $(m, 1)$ with $m \geq 2$. In absence of surface tension, the marginal stability curves for the different waves are very close to each other, so many different waves will become unstable at the same time. With surface tension, the high m modes are much less destabilized and there is a clear preference for the $(1, 1)$ mode. No waves with smaller radial structures $(n \geq 2)$ can become unstable in the shown part of parameter space.

In figure 5-(a), we visualize the current excesses $\widehat{\boldsymbol{j}}_i$, $\widehat{\boldsymbol{\mathcal{J}}}_i^v$ and $\widehat{\boldsymbol{\mathcal{J}}}_i^h$ that are associated with the fundamental wave $(1, 1)$ and for an equilibrium electrolysis current $\boldsymbol{J}$ that flows from top to bottom. The deformed interface is suggested

(m,n)	k (m^{-1})	ω	$\lambda_v/|JB_z|$	δ_h/J^2	λ_{vv}/B_z^2	λ_{hh}/J^2	δ_{vh}/JB_z	λ_{visc}
$(1,1)^a$	52.6	4.17	$1.19\ 10^{-3}$	5.81×10^{-14}	-66.3	0.207×10^{-14}	-9.58×10^{-7}	$-6.82\ 10^{-2}$
$(2,1)$	87.3	5.37	$1.37\ 10^{-3}$	0.016×10^{-14}	-78.7	-0.871×10^{-14}	-5.31×10^{-7}	$-1.06\ 10^{-1}$
$(3,1)$	120	6.30	$1.48\ 10^{-3}$	$\to 0$	-86.6	-1.59×10^{-14}	-3.56×10^{-7}	$-1.41\ 10^{-1}$
$(1,2)$	152	7.09	$1.76\ 10^{-4}$	$\to 0$	-189	-0.302×10^{-14}	-0.308×10^{-7}	$-5.21\ 10^{-2}$
$(2,2)$	192	7.96	$2.64\ 10^{-4}$	$\to 0$	-185	-0.764×10^{-14}	-0.333×10^{-7}	$-6.14\ 10^{-2}$
$(3,2)$	229	8.70	$3.21\ 10^{-4}$	$\to 0$	-183	-1.200×10^{-14}	-0.318×10^{-7}	$-7.13\ 10^{-2}$
$(1,1)^b$	52.6	5.80	$8.54\ 10^{-4}$	4.17×10^{-14}				$-8.05\ 10^{-2}$
$(2,1)$	87.3	10.2	$7.23\ 10^{-4}$	9.35×10^{-17}		(same as above)		$-1.45\ 10^{-1}$
$(3,1)$	120	15.3	$6.11\ 10^{-4}$	$\to 0$				$-2.20\ 10^{-1}$
$(1,2)$	152	21.1	$5.90\ 10^{-5}$	$\to 0$				$-8.99\ 10^{-2}$
$(2,2)$	192	29.2	$7.19\ 10^{-5}$	$\to 0$		(same as above)		$-1.18\ 10^{-1}$
$(3,2)$	229	37.8	$7.40\ 10^{-5}$	$\to 0$				$-1.48\ 10^{-1}$

 a without surface tension

a without surface tension
b with surface tension $\gamma_{1|2} = 0.5\,\text{N/m}$

TABLE I. Theoretical values for wavenumbers k (in m^{-1}), inviscid frequencies ω (in s^{-1}), relative growth rates λ_v/JB_z (in s^{-1}A^{-1}m^{2}T^{-1}) and frequency shifts δ_h/J^2 (in s^{-1}A^{-2}m^4), quasistatic corrections of the growth rate λ_{vv}/B_z^2 (in s^{-1}T^{-2}), λ_{hh}/J^2 (in s^{-1}A^{-2}m^4) and frequency δ_{vh}/JB_z (in s^{-1}A^{-1}m^{2}T^{-1}) and viscous damping term λ_{visc} (in s^{-1}) of different waves (m,n) in a small cell with dimensions $R = .035$ m, $H_1 = 0.075$ m, $H_2 = 0.075$ m.

(a) without surface tension $\gamma_{1|2} = 0$

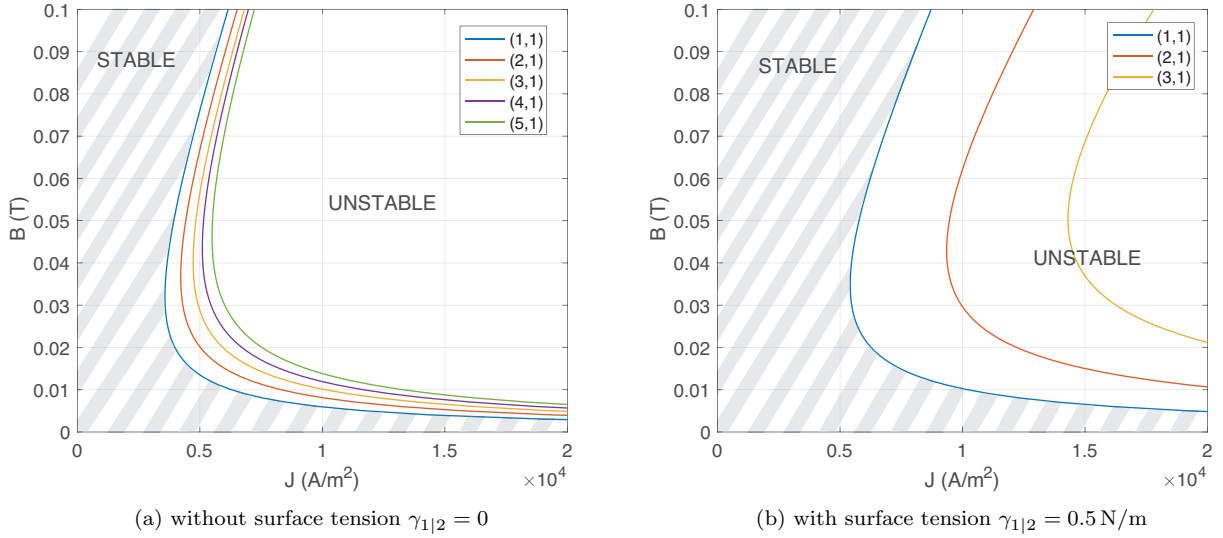(b) with surface tension $\gamma_{1|2} = 0.5\,\text{N/m}$

FIG. 4. Marginal stability curves for metal pad roll instability of waves (m,n) with and without surface tension. In the diagonally barred regions the cell is stable. The large scale sloshing wave $(m,n) = (1,1)$ always becomes unstable first.

by the black line. The current lines $\widehat{\boldsymbol{j}}_i$, due to the interface motion, loop in a symmetrical way in both fluid layers. The quasi-static corrections $\widehat{\boldsymbol{\mathcal{J}}}_i^v$, $\widehat{\boldsymbol{\mathcal{J}}}_i^h$ on the other hand, loop inside the Aluminium and remain well away from the boundaries so that the approximatively isolating boundary conditions are well verified. In panel (b), we plot power densities

$$\widehat{\boldsymbol{u}}_i^* \cdot \left(\widehat{\boldsymbol{j}}_i \times B_z \boldsymbol{e}_z \right) \quad , \quad \widehat{\boldsymbol{u}}_i^* \cdot \left(\widehat{\boldsymbol{\mathcal{J}}}_i^v \times B_z \boldsymbol{e}_z \right) \quad , \quad \widehat{\boldsymbol{u}}_i^* \cdot \left(\widehat{\boldsymbol{\mathcal{J}}}_i^h \times (\mu_0 Jr/2\boldsymbol{e}_\theta) \right) + \mu_0 J \widehat{\phi}_i^* \widehat{u}_{i,z} \tag{83}$$

that appear in the integranda of $\mathcal{P}_v$, $\mathcal{Q}_{vv}$ and $\mathcal{Q}_{hh}$. This allows to visually locate where the instability is powered or inversely where magnetic damping can take place. In this small cell configuration, we see that both the Cryolite and the Aluminium participate in a symmetric way in the destabilization through $\mathcal{P}_v$. The density that defines $\mathcal{Q}_{vv}$ is

(a) streamlines of current densities
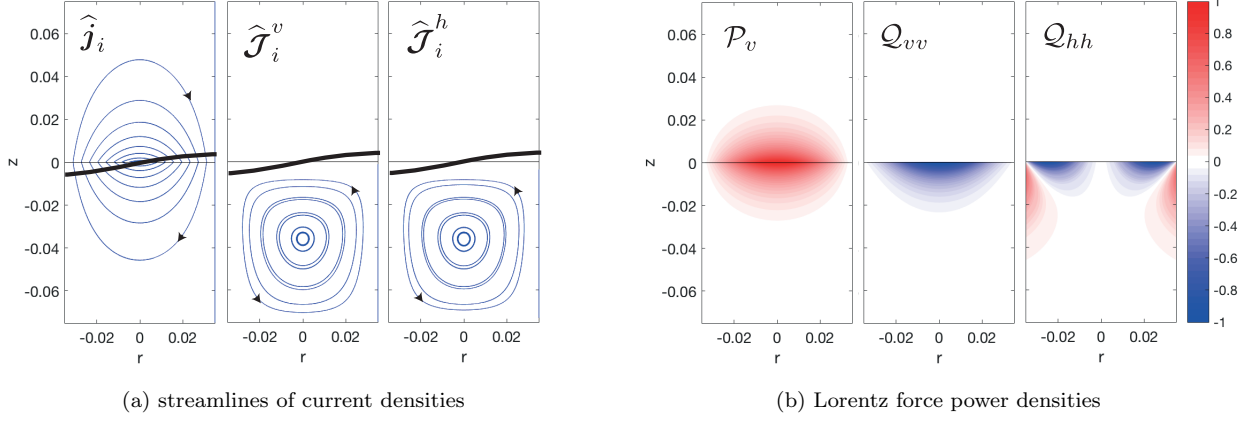
(b) Lorentz force power densities

FIG. 5. Small cell geometry. Current excess lines together with normalized power density plots for the fundamental wave $(1,1)$. The interface deformation is suggested by the thick black line. The magneto-static current perturbation $\widehat{\boldsymbol{j}}_i$ driven by the motion of the interface motion exists in both fluid layers, quasi-static corrections $\widehat{\boldsymbol{\mathcal{J}}}_i^v$ and $\widehat{\boldsymbol{\mathcal{J}}}^h$ loop in the Aluminium layer where the conductivity is higher.

(m,n)	model	ω	λ_v/JB_z	λ_{vv}/B_z^2	λ_{visc}
$(1,1)$	exact	4.169	$1.189\ 10^{-3}$	-66.3	-0.0682
"	deep	4.171	$1.185\ 10^{-3}$	-	-0.0684
"	shallow	8.284	$1.513\ 10^{-4}$	-64.2	-0.0245
$(2,1)$	exact	5.372	$1.370\ 10^{-3}$	-78.7	-0.1056
"	deep	5.372	$1.370\ 10^{-3}$	-	-0.1056
"	shallow	13.740	$8.184\ 10^{-3}$	-98.0	-0.0315

TABLE II. Comparison of exact theoretical formula with deep and shallow limits for inviscid frequencies ω (in s^{-1}), relative growth rates λ_v/JB_z (in s^{-1}A^{-1}m^{2}T^{-1}), relative damping term λ_{vv}/B_z^2 (in s^{-1}T^{-2}), viscous damping rates λ_{visc} (in s^{-1}). Surface tension is ignored. For the small cell under study, the deep formula provide a very accurate description as opposed to the shallow limit formula, which is not well adapted.

negative in the bottom Aluminium layer where the flow induction may take place. Although $\mathcal{Q}_{hh}$ is negligibly small in this small reduction cell, we notice that

$$\underbrace{\widehat{\boldsymbol{u}}_i^* \cdot \left(\widehat{\boldsymbol{\mathcal{J}}}_i^h \times (\mu_0 Jr/2\boldsymbol{e}_\theta) \right)}_{<0} + \underbrace{\mu_0 J\widehat{\phi}_i^* \widehat{u}_{i,z}}_{>0} \tag{84}$$

in the power-density that determines Q_{hh} (panel (b), right plot). The first term is stabilizing (<0, blue spots) and the second is destabilizing (>0 red spots). Both terms do not operate at the same place in space.

In the theoretical section, we have provided exact formulas for the frequency ω and growth rate λ_v (48) together with deep and shallow limits. In table II, we apply the different formulas to the case of this small cell. We focus on two waves $(m,n) = (1,1), (2,1)$ and ignore surface tension. The deep limit formula (50) clearly provides an excellent approximation, which is not really a surprise considering that the small cell is rather tall (see figure 3-(a)). The shallow-limit formulas (52) are not adapted to capture the metal pad roll instability in this cell.

In table III we compare the theoretical calculation of λ_{vv}/B_z^2 using formula (72) to numerically calculated values. The numerical values are obtained using numerical quadrature and the field profiles $\widehat{\Psi}_i^v$ that result from the finite difference code. Increasing the spatial resolution $M = 100, 200, 400, 800$ in that code, we observe how the values of the damping rates converge towards the theoretical prediction of (72). This validates our finite difference solver, but also suggests that (72) provides an excellent description of the magnetic damping rate.

In figure 6, we study how λ_v/JB_z and λ_{vv}/B_z^2 of the fundamental wave $(m,n) = (1,1)$ would hypothetically vary with the electrical conductivity of the top (Cryolite) layer. We use the numerical approach to calculate λ_{vv}/B_z^2, since the conductivity σ_1 varies from the realistic value 250 S/m up to $\sigma_1 = \sigma_2$ so that the top layer will participate in

(m,n)	num $(100)^a$	num (200)	num (400)	num (800)	theoretical^b
$(1,1)$	-66.47	-66.37	-66.34	-66.33	-66.31
$(2,1)$	-79.08	-78.82	-78.76	-78.75	-78.71
$(3,1)$	-87.19	-86.77	-86.66	-86.63	-86.60

[a] numerical calculations of λ_{vv}/B_z^2 for varying grid-size
[b] theoretical calculation of λ_{vv}/B_z^2 using (72)

TABLE III. The relative magnetic damping rates λ_{vv}/B_z^2 (in $\mathrm{s}^{-1}\mathrm{T}^{-2}$) for different waves (m,n) can be calculated numerically using a finite finite difference solver with variable spatial resolution $M = 100, 200, 400, 800$ or theoretically, using (72). The numerical values converge towards the theoretical estimate.

(a) growth rate
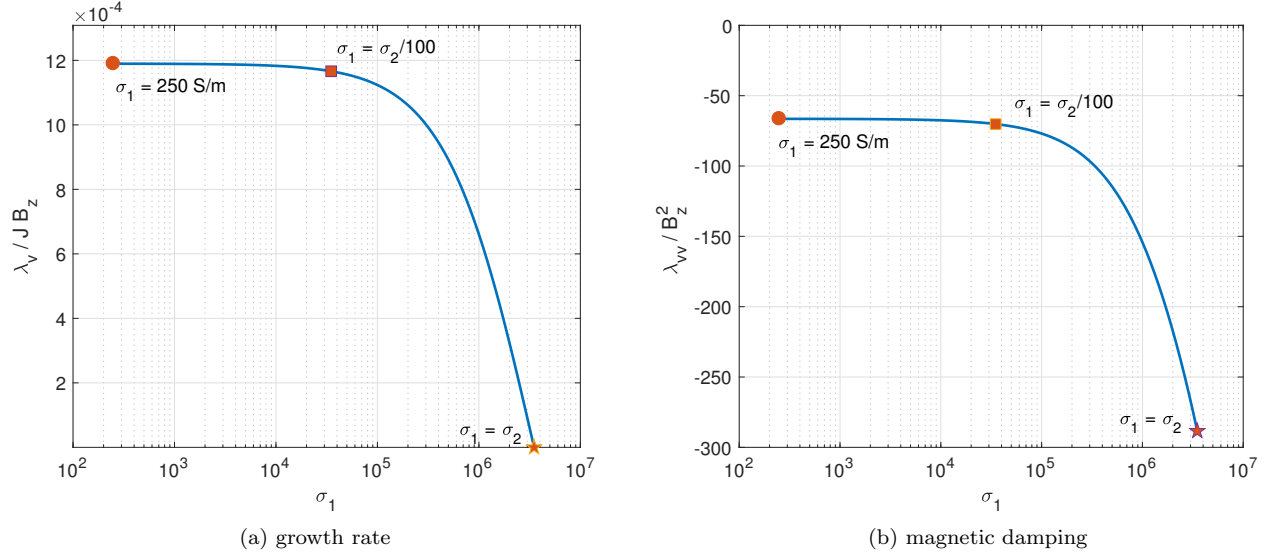
(b) magnetic damping

FIG. 6. Variation of the relative growth rate λ_v/JB_z (panel (a)) and magnetic damping term λ_{vv}/B_z^2 (panel (b)) when σ_1 is artificially increased. From $\sigma_1 = 250\,\mathrm{S/m}$ to $\sigma_1 = \sigma_2/100$ there is only a weak modification of the growth rate and magnetic damping. This suggests that, in direct numerical simulations, one can significantly relax the conductivity jump, without modifying the linear instability characteristics. At $\sigma_1 = \sigma_2$, the instability vanishes: a strong difference in conductivity is essential for the metal pad roll instability.

the damping. From $\sigma_1 = 250\,\mathrm{S/m}$ towards $\sigma_1 = \sigma_2/100$, we observe little changes in both λ_v/JB_z and λ_{vv}/B_z^2. The conductivity of the electrolyte can be significantly increased without modifying the essence of the instability mechanism and the magnetic damping rate. A further increase of σ_1 does affect the instability, that even vanishes at $\sigma_1 = \sigma_2$. There can be no metal pad roll instability without a significant jump in conductivity.

2. Numerical results & comparison

The numerical study is done with SFEMaNS and OpenFOAM and ignoring surface tension. In both codes, we have varied the grid-size to assess the numerical convergence. We introduce the non-dimensional measure $h = \delta x/R$ to characterize the grid size. In SFEMaNS the cell-size δx is non-uniform in the plane (r, z) and the cells are refined near the interface. Therefore we provide intervals $h = (h_{\min} \to h_{\max})$ to characterize the SFEMaNS grid. All the simulations reported in the paper have been done with 30 real Fourier modes in the azimuthal direction. In SFEMaNS, we relax the conductivity jump by taking $\sigma_1 = \sigma_2/100$. This stabilizes the numerical calculations and as explained above, should not modify the linear instability mechanism. In OpenFOAM only purely orthogonal cells are used with $h = 0.05$ or smaller. The cells are flattened towards the interface with an aspect ratio of 5 at most. Interface compression ensures that the interface is typically smeared over 2-3 cells.

In a first series of tests, we put $J = 0$, $B_z = 0$, initialize the numerical simulations with low amplitude gravity wave

wave $(m,n) = (1,1)$	h	$\omega + \delta_{visc}$	λ_{visc}	λ_{vv} (10 mT)	λ_{vv} (25 mT)	λ_{vv} (50 mT)
SFEMaNS	$(0.86 \to 5) \times 10^{-2}$	4.086	-0.0773	-0.1032	-0.1375	-0.2480
	$(0.43 \to 5) \times 10^{-2}$	4.101	-0.0805	-0.0066	-0.0412	-0.1533
	$(0.2 \to 5) \times 10^{-2}$	4.096	-0.0805	-0.0069	-0.0421	-0.1539
OpenFOAM	5.00×10^{-2}	4.078	-0.0519	-0.0071	-0.0404	-0.1527
	4.00×10^{-2}	4.078	-0.0590	-0.0053	-0.0401	-0.1511
	3.33×10^{-2}	4.105	-0.0646	-0.0056	-0.0387	-0.1507
	2.50×10^{-2}	4.102	-0.0678	-	-	-
	2.00×10^{-2}	4.107	-0.0717	-	-	-
	1.539×10^{-2}	4.104	-0.0724	-	-	-
Theory		4.101	-0.0682	-0.0066	-0.0414	-0.1658

wave $(m,n) = (2,1)$	h	$\omega + \delta_{visc}$	λ_{visc}	λ_{vv} (10 mT)	λ_{vv} (25 mT)	λ_{vv} (50 mT)
SFEMaNS	$(0.86 \to 10.7) \times 10^{-2}$	5.087	-0.1981	-0.0039	-0.0331	-0.1290
	$(0.43 \to 5) \times 10^{-2}$	5.150	-0.1251	-0.0084	-0.0478	-0.1807
	$(0.2 \to 5) \times 10^{-2}$	5.084	-0.1236	-0.0085	-0.0473	-0.1804
Theory		5.267	-0.1056	-0.0079	-0.0492	-0.1968

TABLE IV. In absence of electrolysis current and without surface tension, gravity waves are damped by viscous and magnetic dissipation. Using both SFEMaNS and OpenFOAM, we simulate the decay of large scale gravity waves $(m,n) = (1,1), (2,1)$ with or without imposed magnetic field $B_z = 0, 10, 25, 50$ mT and using different grids wih typical mesh-sizes $h = \delta x/R$. We measure the frequency $\omega + \delta_{visc}(\mathrm{s}^{-1})$, the viscous damping rate $\lambda_{visc}(\mathrm{s}^{-1})$ and the magnetic damping rates $\lambda_{vv}(\mathrm{s}^{-1})$ of the waves and we compare with the theoretical estimates provided by the perturbative analysis.

profiles for $(m,n) = (1,1), (2,1)$ and let these waves decay in time. We measure numerical values for the frequency and viscous damping rates of these waves and compare these measures with the viscously corrected frequency $\omega + \delta_{visc}$ and damping rate λ_{visc} of our theoretical model. All results are gathered in table IV. Both solvers OpenFOAM and SFEMaNS clearly show convergence in gravity wave frequency $\omega + \delta_{visc}$ as the grid is refined and the measured frequencies closely match with the theoretical value. For the fundamental wave $(1,1)$, the absolute error between theory and numerics reaches levels of $0.01\,\mathrm{s}^{-1}$ and relative errors of the order of $2.4\,10^{-3}$. For the wave $(m,n) = (2,1)$ there is a larger mismatch but the agreement still is very good. For the viscous damping rates λ_{visc}, we also observe convergence in both codes as the grid is refined. Waves are slightly more damped in the numerical simulations than predicted by theory and there is a noticeable difference between both codes: the same waves are more viscously damped in SFEMaNS than in OpenFOAM. The OpenFOAM measure is closer to theoretical estimate, but we must remind that theory is also slightly uncertain due to the neglected contact line effects.

In a second series of tests, we measure the damping rates of gravity waves in presence of non-zero external magnetic fields $B_z \neq 0$, without electrolysis current $(J = 0)$. We do simulations for increasing magnetic field $B_z = 10, 25, 50$mT. If λ denotes the (negative) growth rate of the waves in the numerical simulations using a mesh with cell-size h and λ_{visc} the viscous growth rate measured for this mesh, we then calculate numerical values $\lambda_{vv} = \lambda - \lambda_{visc}$ in order to filter the code- and grid-dependent viscous damping that was considered in the previous section. Table IV gathers numerical measures for λ_{vv} that can be compared with the theoretical estimates for waves $(1,1), (2,1)$. The agreement with the theoretical value is very good but clearly requires a sufficiently fine grid. For the lower $B_z = 10, 25\,\mathrm{mT}$, there is an excellent agreement. For high $B_z = 50\,\mathrm{mT}$ there is a small mismatch that we accredit to the fact that we are leaving the asymptotical regime of validity of the theoretical model. We note that the magnetic damping rates $-\lambda_{vv}$ are slightly lower in OpenFOAM than in the simulations done with SFEMaNS.

In a third series of tests, we perform simulations of the metal pad roll instability with both J and B_z present. We fix the magnetic field strength to $B_z = 16\,\mathrm{mT}$ previously used by [23] in a similar small reduction cell. We increase the current density in the interval $J \in -[7795, 25984]\,\mathrm{A\,m}^{-2}$ that corresponds to electrolysis currents of $I = [30, 100]$A, running downwards through the cell. From theory, we can estimate that metal pad roll instability should occur when $|J|$ is above a threshold current density located at $J_c = 4476\,\mathrm{A\,m}^{-2}$. In figure 7, we show that metal pad roll instability indeed sets in when $|J| = 7795\,\mathrm{A/m}^2 > \mathrm{J_c}$ and in both numerical codes. We have plotted the interface deformation during one rotation period of the saturated rotating wave, which clearly is dominated by the fundamental $(m,n) = (1,1)$ wave rotating in anti-clockwise direction $(m\omega < 0)$, when seen from above. This corresponds to what
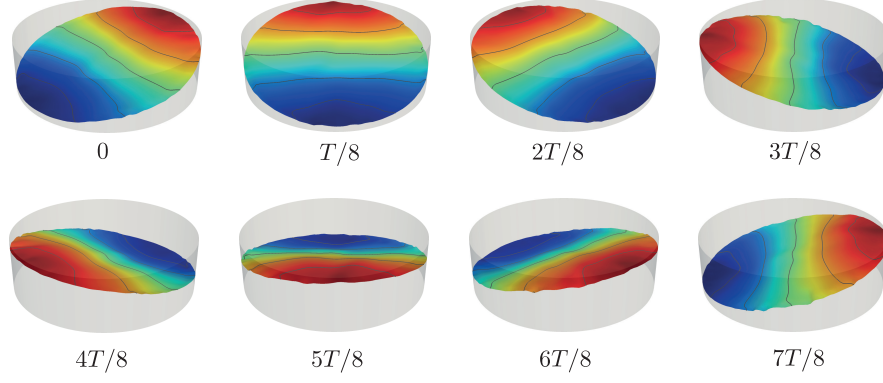
(a) Weakly nonlinear regime (OpenFOAM)
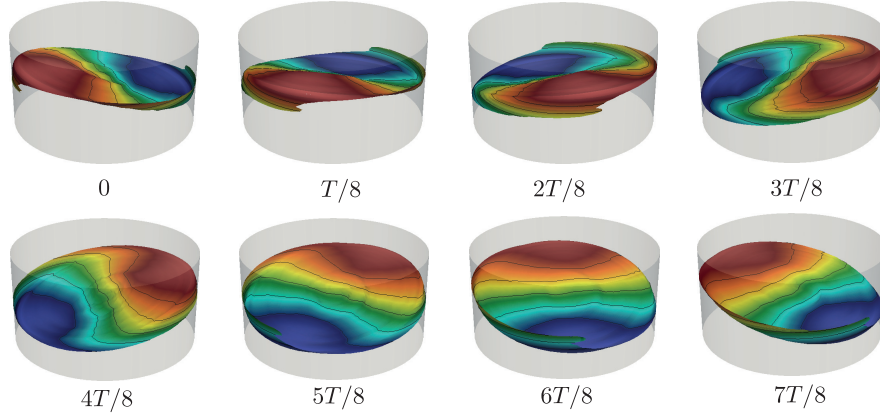
(b) Weakly nonlinear regime (SFEMaNS)
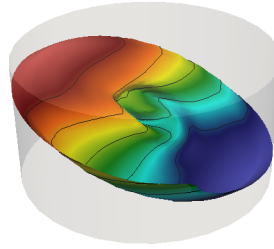
(c) Strongly nonlinear
regime (SFEMaNS)

FIG. 7. Visualisaton of the interface between the Cryolite and Aluminum in the numerical simulations. (a) and (b) show the weakly nonlinearly regime in which a rotating gravity wave saturates in magnitude. 8 snapshots are shown over one period T of the large scale sloshing wave $(m, n) = (1, 1)$. $J = -7795 \, \mathrm{A/m}^2$, $B_z = 16 \, \mathrm{mT}$. (c) Further away from threshold, the interface may violently destabilize and develop large deformations, here for $J = -20000 \mathrm{A/m}^2$, $B_z = 16 \, \mathrm{mT}$.

can be expected from the theory and from the Sele-mechanism [2]. In a more systematic series of computations we have measured the growth rate of the metal pad roll instability as a function of J. They are plotted in figure 8(a) next to the theoretical estimate $\lambda \approx \lambda_v + \lambda_{vv} + \lambda_{visc}$. We observe an excellent agreement with the theoretical line that, we remember, grows linearly because $\lambda_v \sim |JB_z|$. The fact that both codes find straight lines with the same slope is an indication that both codes capture the destabilizing mechanism behind λ_v very well. The SFEMaNS growth rates are slightly beneath the OpenFOAM values, which is not unexpected owing to the small difference in viscous damping rates (from table IV: $\lambda_{visc} \approx -0.0805$ (SFEMaNS), $\lambda_{visc} \approx -0.0678$ (OpenFOAM, $h = 0.025$)).
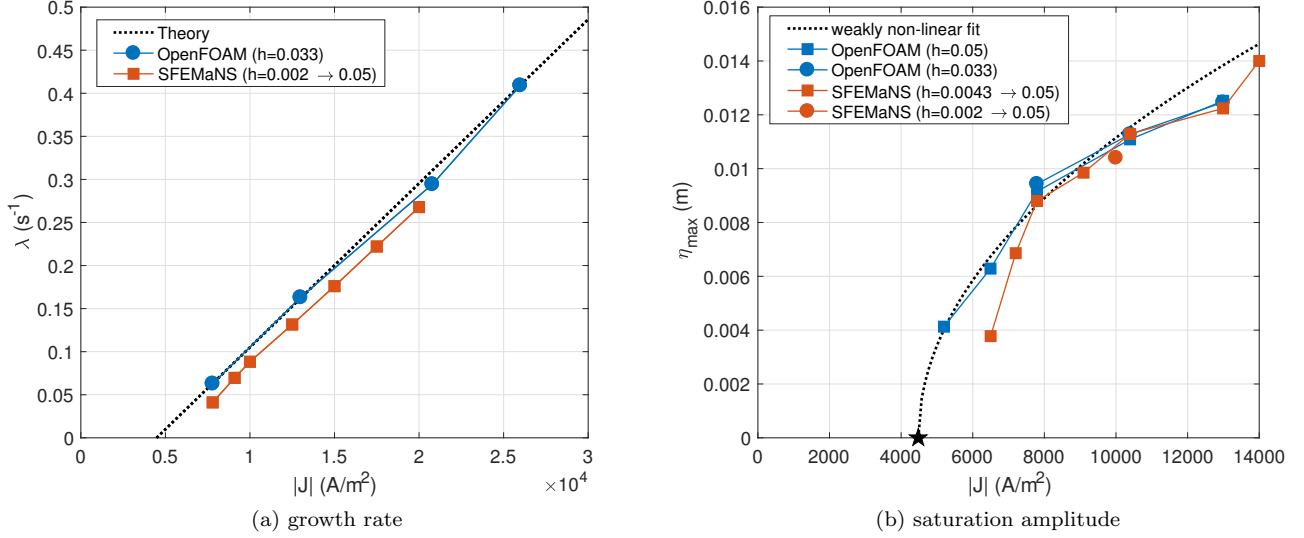
(a) growth rate

(b) saturation amplitude

FIG. 8. (a) Comparison of theoretical and numerical growth rates for the large scale sloshing wave $(m, n) = (1, 1)$ as a function of $|J|$. (b) Saturation amplitudes of rotating wave as a function of $|J|$. Small cell configuration with $B_z = 16$ mT and ignoring surface tension.

The numerical simulations further provide insights in the nonlinear regime, not modeled by our theory. In figure 8(b), we show a diagram that gathers maximal amplitudes $\eta_{\max}$ of saturated rotating gravity waves as a function of current density. This suggests a supercritical bifurcation. We can propose a weakly nonlinear fit $\eta_{\max} = 1.5 \times 10^{-4} \sqrt{|J| - J_c}$ in MKSA units (based on the OpenFOAM data). In non-dimensional form and using the theoretical formula for the growth rate λ, we can rewrite this fit as

$$\text{If } \lambda > 0 \quad : \quad \frac{\eta_{\max}}{R} \approx 2 \sqrt{\frac{\lambda}{|\omega|}} \tag{85}$$

In the perturbative limit, the weakly nonlinear saturation process is mainly hydrodynamical. Therefore, we expect that this non-dimensional relation is more generally applicable to estimate the weakly nonlinear saturation amplitudes of the fundamental wave $(1, 1)$ in tall (deep) reduction cells. The task of finding a theoretical confirmation of this law would be formidable, but is out of scope here.

The weakly nonlinear regime exists in a limited parameter range. When we push the electrical current density even higher, above $|J| \sim 15000 \, \text{A/m}^2$, we can get violent secondary instabilities with both numerical solvers. The interface undergoes strong deformations which ultimately lead to a blow up of the numerical calculation. To illustrate this phenomenon, we show in figure 7(c) the interface obtained with $J = -20000 \, \text{A/m}^2$ using SFEMaNS. The origin of this secondary instability is unknown, but similar explosive behavior was also observed in liquid metal battery geometry [35, 36].

B. Large, industrial scale cells

In this section, we apply the theory to investigate metal pad roll instability in large, industrial scale cells, with $H_1 = 0.05 \, \text{m}$, $H_2 = 0.30 \, \text{m}$ and large radii $R \in [0.5, 2.5] \, \text{m}$, so that we can ignore surface tension.

In Table V we provide numerical values for all the relevant quantities determining the stability and frequency shifts of different waves (m, n) in a $R = 1 \, \text{m}$ cell. As in the small cell, axisymmetric waves, with $m = 0$ are never unstable. In the column for λ_v/JB_z, we see that the fundamental wave $(1, 1)$ will always be the most destabilized wave, by far. Since viscous dissipation is also lowest for this wave, we can expect to see predominantly this wave. The relative frequency shift δ_h/J^2 can be either positive or negative and decays as m or n increase. Although the numbers are small, this effect will no longer be negligible for current densities of the order $J \sim 10^4 \, \text{A m}^{-2}$). For the quasi-static corrections λ_{vv}/B_z^2, λ_{hh}/J^2 and δ_{vh}/JB_z we find the same trends as in the small cell. With $\lambda_{hh}/J^2 = 8.06 \times 10^{-14}$ we can seemingly have a very weak destabilization of the wave $(1, 1)$ even with $B_z = 0$. However, unrealistic currents of

(m,n)	k	ω	λ_v/JB_z	δ_h/J^2	λ_{vv}/B_z^2	λ_{hh}/J^2	δ_{vh}/JB_z	λ_{visc}
$(1,1)$	1.84	0.31	1.79×10^{-3}	2.27×10^{-10}	-18.8	8.06×10^{-14}	-0.45×10^{-6}	-0.77×10^{-2}
$(2,1)$	3.05	0.51	1.01×10^{-3}	0.58×10^{-10}	-28.8	-0.11×10^{-11}	-0.94×10^{-6}	-0.98×10^{-2}
$(3,1)$	4.20	0.69	0.73×10^{-3}	-0.07×10^{-10}	-36.2	-0.31×10^{-11}	-1.38×10^{-6}	-1.13×10^{-2}
$(1,2)$	5.33	0.85	0.07×10^{-3}	1.21×10^{-10}	-104	-0.08×10^{-11}	-0.20×10^{-6}	-1.07×10^{-2}
$(2,2)$	6.71	1.05	0.08×10^{-3}	0.86×10^{-10}	-105	-0.27×10^{-11}	-0.32×10^{-6}	-1.12×10^{-2}
$(3,2)$	8.02	1.22	0.09×10^{-3}	0.64×10^{-10}	-109	-0.51×10^{-11}	-0.39×10^{-6}	-1.14×10^{-2}

TABLE V. Theoretical values for wavenumbers k (in m^{-1}), inviscid frequencies ω (in s^{-1}), relative growth rates λ_v/JB_z (in s^{-1}A^{-1}m^{2}T^{-1}) and frequency shifts δ_h/J^2 (in s^{-1}A^{-2}m^4), quasistatic corrections of the growth rate λ_{vv}/B_z^2 (in s^{-1}T^{-2}), λ_{hh}/J^2 (in s^{-1}A^{-2}m^4) and frequency δ_{vh}/JB_z (in s^{-1}A^{-1}m^{2}T^{-1}) and viscous damping term λ_{visc} (in s^{-1}) of different waves (m,n) in a large cell with dimensions $R = 1$ m, $H_1 = 0.05$ m, $H_2 = 0.3$ m. Surface tension is ignored.
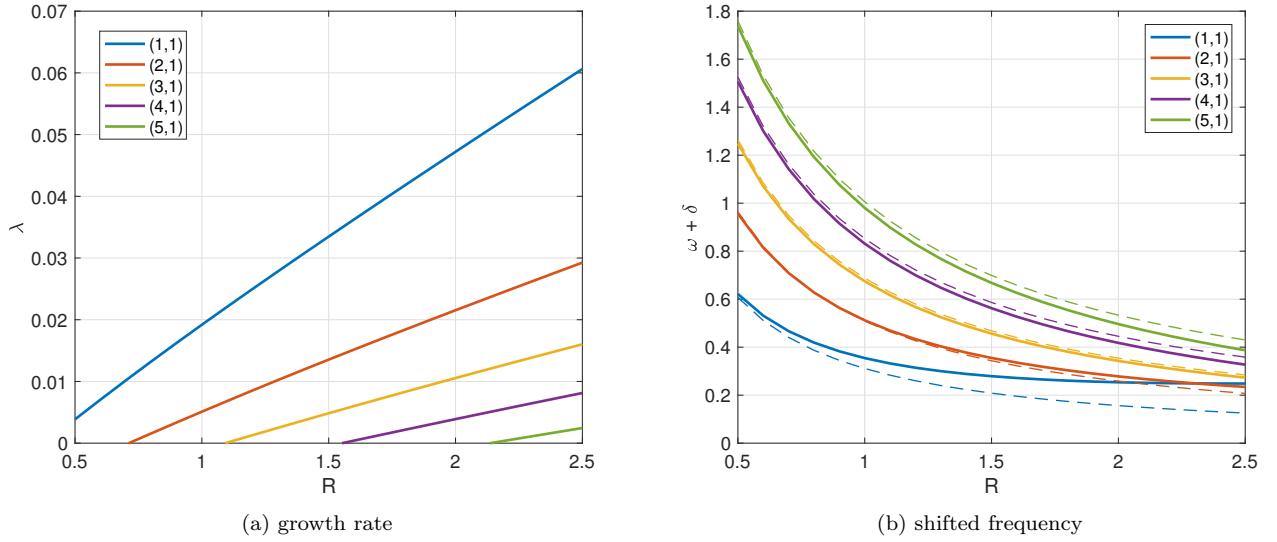

(a) growth rate

(b) shifted frequency

FIG. 9. Growth rate λ and shifted frequency $\omega + \delta$ of various gravity waves (m,n) in large cells with varying radius. Dimensions are $R \in [0.5, 2.5]$m, $H_1 = 0.05$m, $H_2 = 0.35$m and we take realistic values for current density and vertical magnetic field $J = 1.5 \times 10^4$A m^{-2} and $B_z = 1$mT. The dashed lines in panel (b) correspond to the unperturbed gravity wave frequency ω and allow to see the impact of the shift δ.

the order of $|J| > 3.1 \times 10^5$A m^{-2} would still be required to overcome the weak viscous dissipation λ_{visc}. Furthermore, at such high values of J, we surely violate $\delta_h \ll \omega$ by far and one necessary condition for using perturbation methods is then violated so that our model likely is no longer valid in that very high J-range. It seems safe to say that this strange destabilization is anecdotical in real life.

We fix $J = 1.5 \times 10^4$ A m^{-2} and $B_z = 1$mT to realistic values and let the radius of the cell vary in the range $R \in [0.5, 2.5]$ m. Due to the low vertical magnetic field strength and the low values of λ_{hh}/J^2 we can neglect all quasi-static MHD effects in the large cell and use

$$\lambda \approx \lambda_v + \lambda_{visc} \quad , \quad \delta \approx \delta_h + \delta_{visc} \tag{86}$$

as a suitable approximation. Figure 9 displays how the growth rate λ and the shifted frequency $\omega + \delta$ vary with R. In panel (a), we clearly see that the growth rate increases linearly with R, in agreement with the shallow limit formula (54). The large scale sloshing mode $(1,1)$ always remains the most unstable mode even for the very big cells. In panel (b), the dashed lines show that the inviscid frequency ω decays with R. This is coherent with theory that predicts $\omega_{shallow} \sim R^{-1}$. The full lines show the shifted frequency, $\omega + \delta$ that clearly deviate from ω. This shift is here mostly due to the δ_h, i.e. caused by the Lorentz-force interaction of electrical currents $\hat{\boldsymbol{j}}_i$ with the horizontal magnetic field $\mu_0 J r/2\, \boldsymbol{e}_\theta$. Note finally, that $\lambda \ll \omega$ and $\delta \ll \omega$ seem verified for all but the largest cells, which suggests that perturbation methods may be applicable to model realistically large reduction cells.

(m,n)	model	ω	λ_v/JB_z	λ_{vv}/B_z^2	λ_{visc}	δ_h/J^2
$(1,1)$	exact	0.311	1.79×10^{-3}	-18.83	-0.767×10^{-2}	2.27×10^{-10}
"	shallow	0.314	1.75×10^{-3}	-18.79	-0.751×10^{-2}	2.30×10^{-10}
$(2,1)$	exact	0.508	1.01×10^{-3}	-28.78	-0.983×10^{-2}	0.58×10^{-10}
"	shallow	0.521	0.95×10^{-3}	-28.70	-0.967×10^{-2}	0.59×10^{-10}

TABLE VI. Comparison of exact theoretical formula with shallow limits for inviscid frequencies ω (in s^{-1}) and relative growth rates λ_v/JB_z (in s^{-1}A^{-1}m^{2}T^{-1}), relative magnetic damping term λ_{vv}/B_z^2 (in s^{-1}T^{-2}), viscous damping term λ_{visc} (in s^{-1}) and relative frequency shift δ_h/J^2 (in s^{-1}A^{-2}m^4). In the large cell under study, the shallow limit formula provide a very accurate description.

(a) streamlines of current densities
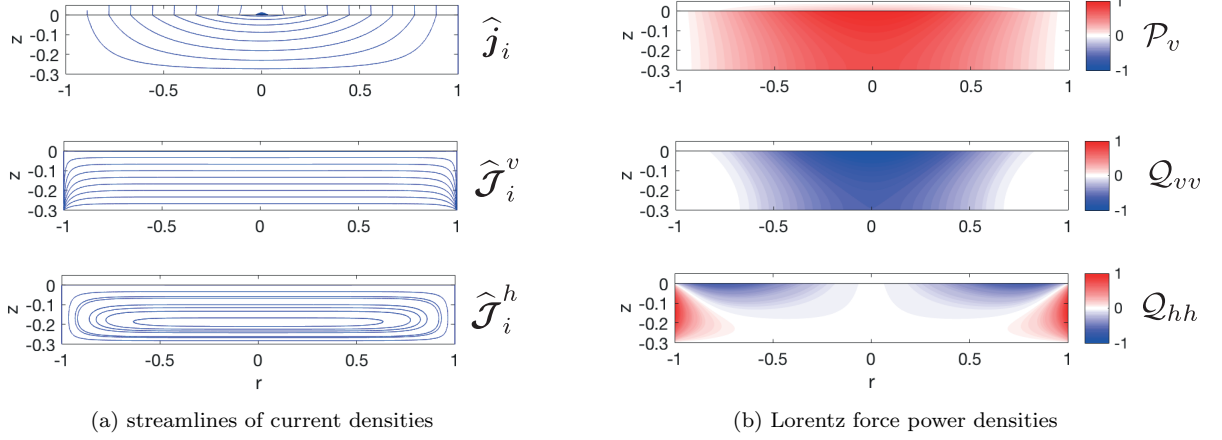

(b) Lorentz force power densities

FIG. 10. Large cell geometry $R = 1m$. Current excess lines together with normalized power density plots for the fundamental wave $(1,1)$.

In figure 10, we visualize the current excesses $\widehat{\boldsymbol{j}}_i$, $\widehat{\boldsymbol{\mathcal{J}}}_i^v$, $\widehat{\boldsymbol{\mathcal{J}}}_i^h$ together with the power densities (83) in a similar way as to what we did in figure 10 for the small cell. In panel (a), we see that $\widehat{\boldsymbol{j}}_i$ is mainly vertical in the electrolyte and horizontal in the Aluminium. This is remarkably different from what we had in the small cell, but also corresponds to what was assumed in all available shallow layer descriptions of metal pad roll instability. Even though $\widehat{\boldsymbol{\mathcal{J}}}_i^v$ and $\widehat{\boldsymbol{\mathcal{J}}}_i^h$ have negligible impact, it is recomforting to see that these currents are also almost horizontal and remain well within the Aluminium layer. In panel (b), we plot the power densities (83) that enter in the definition of $\mathcal{P}_v$, $\mathcal{Q}_{vv}$ and $\mathcal{Q}_{hh}$. Contrary to the small cell, we see that destabilization through $\mathcal{P}_v$ is mainly powered in the bottom layer where the currents $\widehat{\boldsymbol{j}}_i$ are horizontal.

V. APPLICATION TO A LIQUID METAL BATTERY

In [35, 36], the metal pad roll instability was numerically studied in Mg$||$NaCl $-$ KCl $-$ MgCl$_2||$Sb liquid metal batteries (LMBs). In these batteries there are not two, but three layers of conducting fluid, with the following material properties

$$(\rho_1, \rho_2, \rho_3) = (1577, 1715, 6270)\,\text{kg m}^{-3}$$
$$(\sigma_1, \sigma_2, \sigma_3) = (3.6\,.10^6, 80, 8.7\,.10^5)\,\text{S m}^{-1}$$
$$(\nu_1, \nu_2, \nu_3) = (6.7, 6.8, 2.0)\,.10^{-7}\,\text{m}^2\,\text{s}^{-1}$$

$$(87)$$

and interfacial tensions

$$(\gamma_{1|2}, \gamma_{2|3}) = (0.19, 0.095)\,\text{N m}^{-1}. \tag{88}$$

(a) simulation of metal pad roll in Mg-Sb
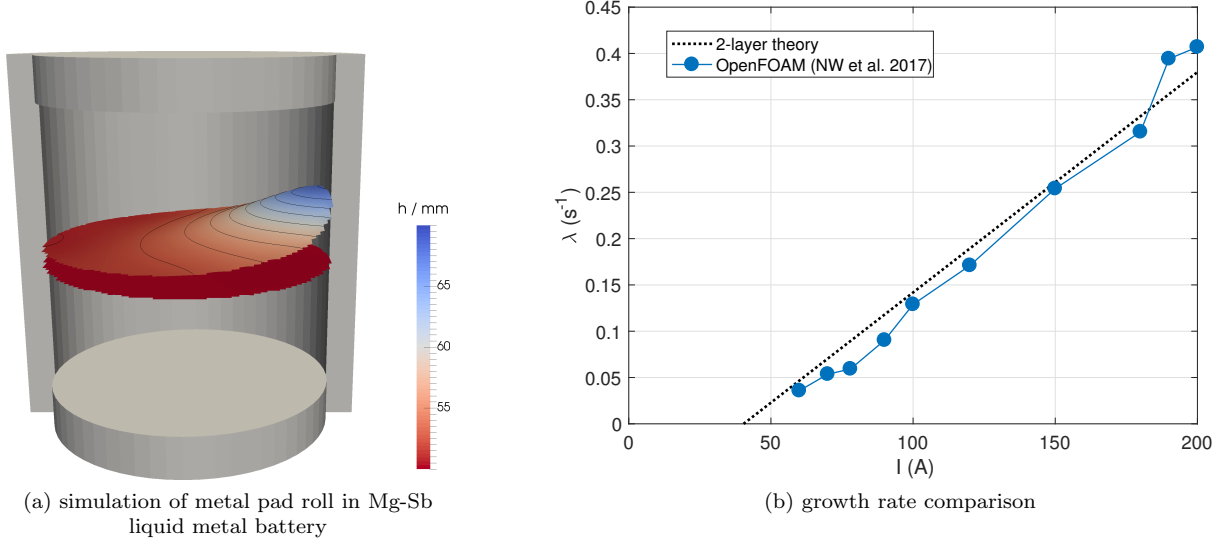liquid metal battery

(b) growth rate comparison

FIG. 11. (a) snapshot of a numerical simulations the metal pad roll instability in Mg-Sb liquid metal battery. $J = 10^4 \, \text{A m}^{-2}$, $B_z = 10\text{mT}$. (b) Growth rate of the metal pad roll instability in the numerical simulations and according to our two-layer theory.

Top (Mg) and bottom (Sb) layers 1 and 3 are very good conductors, but the middle layer 2 ($\text{NaCl} - \text{KCl} - \text{MgCl}_2$) is a badly conducting molten salt electrolyte. [35] performed a series of numerical simulations for $B_z = 10\,\text{mT}$ and for varying electrical currents $I = J\pi R^2$ passing through a cylindrical cell with dimensions.

$$R = 0.05\,\text{m} \quad , \quad (H_1, H_2, H_3) = (0.045, 0.01, 0.045)\,\text{m} \tag{89}$$

Metal pad roll instability was found and growth rate measurements were published. It was observed that due to the large density jump between layers 2 and 3, the motion mainly deforms the upper interface, separating layers 1 and 2. The lower interface only slightly deforms and doesn't really participate and this could also be seen in the frequency of the wave that matched very closely that of the two layer system (only 1 and 2). This motivated us to try to apply our two layer theory to this 3-layer cell system.

The following "technical" operations are necessary in order to apply the theory. We entirely ignore region 3 and all what may occur there. This is a valid hypothesis, since with significant interface motion there will be no contribution to the destablizing and stabilizing mechanisms there. At the 2|3 interface, the electrical boundary condition, as seen from the electrolyte is very similar to the one we had on the top cap of our cylindrical Hall-Heroult cell: the electrolyte encounters there a much better conductor which we can idealize as perfect. This means that if we interchange regions $1 \leftrightarrow 2$ and inverse the sense of gravity $g \to -g$, we can apply all the previous formula.

In figure 11, we show the result of that quantitive comparison. The dashed line corresponds to our theory, without adjustable parameter. The data-points are those of fig. 9 in [35]. The agreement is surprisingly good.

The fact that we find the right slope with our two-layer theory implies that λ_v is certainly correctly calculated. The threshold also seems approximatively right and suggests that the combined magnetic and viscous damping rates $\lambda_{vv} + \lambda_{visc}$ is also more or less correctly calculated. The magnetic damping λ_{vv} only occurs in the well-conducting Mg layer where fluid is sufficiently moving, so we expect this term to be correct. This implies that λ_{visc} also is nearly correct which is more surprising. The viscous damping rate formula used here was derived by supposing no-slip conditions on both top and bottom walls. Here in this LMB, the true viscous boundary condition at the 2|3 interface formally is not no-slip and should rather be the expression of the continuity of velocity and tangential constraint. Now, considering that the bottom fluid 3 is much more heavy and has at the same a much larger dynamical viscosity $\rho_3 \nu_3$, we may expect that layer 3 is only very weakly entrained by the motion of the salt. Continuity of velocity then suggests a boundary condition that should be close to a no-slip condition :

$$u_{2,r}|_{z=-H_2} \approx 0 \quad , \quad u_{2,\theta}|_{z=-H_2} \tag{90}$$

This explains why we think that also viscous damping is more or less correctly calculated here.

VI.   CONCLUSION

In this article, we have formulated a theoretical model for the metal pad roll instability in cylindrical reduction cells. Using perturbation methods, we have derived analytical formulas for the destabilization, the magnetic damping and the viscous damping of gravity waves in cylinders. Our model is new and very complete, since have overcome all common limitations of metal pad roll theory: no assumptions were made on the shallowness, capillary effects are included, we include viscosity, we went beyond the commonly adopted magneto-static approach and we consider arbitrary fluids. We are confident with all the provided theoretical formulas since they were rigorously tested against numerical calculations of the interaction integrals. From the general formula, we have derived asymptotical expressions for deep and shallow reductions. In the Appendix B, we further demonstrated that our model exactly links to previous shallow and inviscid theories for metal pad rolling in cylindrical geometry.

The theoretical expression for the viscous damping rates was tested in experiments, using an orbital sloshing device, fully described in [38]. We found excellent agreement with our theoretical formula. Improvement is still possible by taking into account damping caused by viscous dissipation near the free interface (reachable) and by finding a better boundary layer model near the moving contact line (difficult).

We have applied our theoretical model to a first type of tiny reduction cell, representative of laboratory scale experiments. This cell was previously numerically studied by [22, 23]. It is so small that it requires huge magnetic fields to destabilize, just as high as the fields used in the experiments of [39, 40]. One particularity of the small cell is that the fundamental wave $(1,1)$ is not the only wave to become unstable nor that is always is the most unstable wave. We have also shown that capillary effects have a very significant impact in small cells. The main advantage of studying a small cell is that high precision direct numerical simulations are possible. As such, the small reduction cell defines a perfect benchmark for any multiphase MHD solver. Our solvers SFEMaNS and OpenFOAM arrive as relatively new players in the area of multiphase MHD codes and both pass here a very demanding test. Both codes yield sensibly the same results. In a detailed cross-comparison of theoretical viscous damping rates, magnetic damping rates and instability growth rates with numerical measures we have found excellent agreement. This type of combined approach was quite long to put into practice but really instructive. It allowed us to gradually perfection and debug our numerical solvers and our theory. We know also have a good knowledge of what is truly required in terms of numerical resolution to perform well-resolved calculations of metal pad rolling with SFEMaNS and OpenFOAM.

For large industrial scale cells we limited ourselves to some theoretical aspects only. A first important point to raise is that even large reductions cells may be modelled using perturbation method in limited parameter regimes. Viscous effects and quasi-static corrections always remain small in large cells in agreement with what is frequently assumed. Our theory predicts that the large scale sloshing mode $(1,1)$ always remains the most unstable wave in large cells by far. The self-generated horizontal magnetic field $\mu_0 Jr/2\,\boldsymbol{e}_\theta$ cannot destabilize waves at first order, but modifies the wave frequencies through δ_h. This has not been tested numerically, but is in agreement with previous findings [3, 7]. We expect that this frequency shift is indeed measurable in large cells. A remarkable detail was that we found that quasi-static effects may destabliize the fundamental wave $(1,1)$ very weakly even in absence of B_z. Numerical application in our study suggests that this unreported phenomenon is negligible thus explaining perhaps why it is so unreported. Probably this phenomenon relates in a weak way to the Tayler instability [29, 31, 32] that also has an inductive origin (quasi-static MHD is necessary), is also caused by the term $\boldsymbol{J} \times \boldsymbol{b}$ and is also only destabilizing for $m = 1$ modes.

We finally also applied our theoretical model to metal pad roll instabilities that can occur in $\mathrm{Mg} - \mathrm{Sb}$ liquid metal batteries. There the bottom layer is so heavy that it doesn't participate actively in the destabilization and stabilization of the gravity waves. With some minimal technical maneuvers that are justified, we find that our model explains very well the numerical measures of the growth rates reported in [35].

This study can have many follow ups. First of all, we think that our new and precise theory really can be used to benchmark multiphase MHD codes and we can invite all other scientists working on the topic to benchmark their multiphase MHD solvers on this small reduction cell set-up. Secondly, it is possible to adapt the method to rectangular geometry in order to propose a theoretical model for the experiments of [39, 40]. The inviscid and magneto-static model certainly exists already, but magnetic and viscous damping are not negligible in that set-up and still need to be included. Thirdly, we plan to extend this two-layer model to three layers of fluid in relation to be able to model the metal pad roll instability in arbitrary liquid metal batteries. As shown by several authors [37, 50, 51], waves on both interfaces may couple more or less depending on the density differences between the layers. To correctly capture the metal pad roll instability in arbitrary liquid metal batteries one must include this possibility. This model is already in the make and we hope to report on this topic soon.

Appendix A: Supplementary information for the analytical calculation of λ_v and δ_h

We provide some extra technical information on the analytical calculation of $\mathcal{P}_v, \mathcal{P}_h, \mathcal{K}$ that fix the growth rate λ_v and the frequency shift δ_h in the quasistatic inviscid limit. With the definition (41) of $\mathcal{K}$ and the expression for $\widehat{\eta}$, we find

$$\mathcal{K} = \left[(\rho_2 - \rho_1)g + \gamma_{1|2}k^2\right] \frac{2\pi|A|^2 k^2}{\omega^2} \int_0^R J_m^2(kr)\, r\, \mathrm{d}r \tag{A1}$$

The radial integral can be evaluated analytically. Using equation (11) of [52], p.-135, together with $J_m'(kR) = 0$ for our surface waves profiles, we have

$$\int_0^R J_m^2(kr)\, r\, \mathrm{d}r = \frac{1}{2k^2}(k^2 R^2 - m^2)J_m^2(kR) \tag{A2}$$

This formula also demonstrates that $(k^2 R^2 - m^2) > 0$, a property that we have used in the text. The volume integral that defines $\mathcal{P}_v$ is transformed into a surface integral by remarking that $\boldsymbol{\nabla}\widehat{\phi}_i^* \cdot (-\sigma_i \boldsymbol{\nabla}\widehat{\varphi}_i \times B_z \boldsymbol{e}_z) = \boldsymbol{\nabla} \cdot [-\sigma_i \widehat{\phi}_i^* \boldsymbol{\nabla}\widehat{\varphi}_i \times B_z \boldsymbol{e}_z)]$ in the integrandum. This yields

$$\mathcal{P}_v = 2\pi(-\mathrm{i}m)B_z \left(\sigma_1 \int_0^{H_1} \widehat{\phi}_1^* \widehat{\varphi}_1|_{r=R}\, \mathrm{d}z + \sigma_2 \int_{-H_2}^0 \widehat{\phi}_2^* \widehat{\varphi}_2|_{r=R}\, \mathrm{d}z\right)$$

$$= \frac{2\pi m J B_z |A|^2 \Lambda}{2\omega} J_m^2(kR) \left[\tanh(kH_1) + (kH_2)\sinh^{-2}(kH_2) + \tanh^{-1}(kH_2)\right] \tag{A3}$$

with Λ defined in (48c). The calculation of the frequency shift δ_h is a bit more tricky since there are much more terms to evaluate. The formula

$$\int_0^R J_m(kr)\partial_r[J_m(kr)]\, r^2\, \mathrm{d}r = \frac{m^2}{2k^2} J_m^2(kR) \tag{A4}$$

is useful to simplify a radial integral that is encountered. We have checked the validity of our analytical formula for λ_v and δ_h by performing numerical calculations of the integrals $\mathcal{P}_v, \mathcal{P}_h, \mathcal{K}$ on a discrete grid.

Appendix B: Linking our growth rate formula for λ_v to existing shallow water models

Both [9] and [10] provide shallow water models for the metal pad roll instability in cylindrical geometry, in the inviscid and magnetostatic limit, ignoring surface tension. Here we show how these models link to our growth rate formula λ_v. We start from the model of [10] and to avoid conflicts in notation, we adapt their formula to our setting. The two-dimensional problem to be solved in the shallow approximation is

$$\partial_{tt}^2 \eta - c^2 \nabla^2 \eta = 0 \quad, \quad \nabla^2 \chi = \overline{\beta}\eta \tag{B1}$$

Here $\eta(r, \theta, t)$ relates to the surface elevation and $\chi(r, \theta, t)$ to the electrical potential. The wave-speed c and parameter $\overline{\beta}$ are defined as

$$c^2 = \frac{(\rho_2 - \rho_1)g}{\rho_1 H_1^{-1} + \rho_1 H_2^{-1}} \quad, \quad \overline{\beta} = \frac{JB_z}{(\rho_2 - \rho_1)gH_1 H_2} \tag{B2}$$

Note that the $\overline{\beta}$ used here is not a non-dimensional number. In the right hand side of the equation for χ of (B1), we find $+\overline{\beta}\eta$ (rather than $-\overline{\beta}\eta$ in [10]) because in the present article, we use the convention that the electrolysis current density is $\boldsymbol{J} = J\boldsymbol{e}_z$ (rather then $\boldsymbol{J} = -J\boldsymbol{e}_z$ in [10]). On the lateral sidewall $r = R$, we need to meet the conditions

$$\partial_r \chi|_{r=R} = 0 \quad, \quad \partial_r \eta|_{r=R} = -R^{-1}\partial_\theta \chi|_{r=R} \tag{B3}$$

Solutions of (B1) take the form

$$\eta = AJ_m(kr)\, e^{\mathrm{i}(m\theta + \omega t)} \quad, \quad \chi = \left(-A\overline{\beta}k^{-2}J_m(kr) + Br^m\right) e^{\mathrm{i}(m\theta + \omega t)} \tag{B4}$$

with $k^2 = \omega^2/c^2$ and A, B arbitrary constants. Note that we choose exponential factors $\exp(\mathrm{i}(m\theta + \omega t))$ just as in the present article (rather then $\exp(\mathrm{i}(m\theta - \omega t))$ in [10]). By expressing the boundary conditions, we can find the dispersion relation, here in non-dimensional form

$$\beta J_{m+1}(\kappa) = -\mathrm{i}\kappa^2 J_m'(\kappa) \tag{B5}$$

with $\kappa = kR$ and

$$\beta = \frac{JB_z}{(\rho_2 - \rho_1)g} \frac{R^2}{H_1 H_2} \tag{B6}$$

the non-dimensional number we have encountered in the shallow limit (see 52a) with $\gamma_{1|2} = 0$. We now find an approximative solution of (B5) in the limit of small $\beta \ll 1$. We propose an expansion

$$\kappa = \kappa^{(0)} + \beta\kappa^{(1)} + O(\beta^2) \tag{B7}$$

inject it into (B5) and expand the dispersion relation using Taylor series in powers of β. At order $O(\beta^0)$, we find the constraint

$$0 = -\mathrm{i}\left(\kappa^{(0)}\right)^2 J_m'(\kappa^{(0)}) \quad \Rightarrow \quad \kappa^{(0)} = \kappa_{mn} \tag{B8}$$

The leading order value of the non-dimensional radial wavenumber takes the same values as the ones we have in our model (see (12)), $\kappa^{(0)} = 0$ is not an option here. At order $O(\beta^1)$, we have the constraint

$$J_{m+1}(\kappa_{mn}) = -\mathrm{i}\left[\kappa^{(1)}\left(\kappa_{mn}\right)^2 J_m''(\kappa_{mn}) + 2\kappa^{(1)}\kappa_{mn} J_m'(\kappa_{mn})\right] \tag{B9}$$

With $J_m'(\kappa_{mn}) = 0$ and using the recurrence relations and the Bessel differential equation we can simplify

$$J_{m+1}(\kappa_{mn}) = \frac{m}{\kappa_{mn}} J_m(\kappa_{mn}) \quad , \quad J_m''(\kappa_{mn}) = -\left(\frac{\kappa_{mn}^2 - m^2}{\kappa_{mn}^2}\right) J_m(\kappa_{mn}) \tag{B10}$$

This yields

$$\mathrm{i}\kappa^{(1)} = \frac{m}{\kappa_{mn}(\kappa_{mn} - m^2)} \tag{B11}$$

The small wavenumber shift $\kappa^{(1)}$ affects the complex frequency ω of the waves as $\omega = \pm\frac{c\kappa}{R}$ by definition in the shallow layer approximation. We propose a small β-expansion of ω

$$\omega = \omega^{(0)} + \beta\omega^{(1)} + O(\beta^2) \tag{B12}$$

and find

$$\omega^{(0)} = \omega_{shallow} = \pm\frac{c\kappa_{mn}}{R} \quad , \quad \omega^{(1)} = \pm\beta\frac{c\kappa^{(1)}}{R} \tag{B13}$$

We recognize $\omega^{(0)}$ as the eigenfrequency $\omega_{shallow}$ of the non-dispersive gravity waves in the shallow layer limit. The complex frequency shift α used in our model is defined as

$$\alpha = \mathrm{i}\omega - \mathrm{i}\omega^{(0)} = \beta\frac{m\omega^{(0)}}{\kappa_{mn}^2 - m^2}\frac{1}{\kappa_{mn}^2} \tag{B14}$$

This exactly coïncides with our shallow limit formula (52a) of the growth rate λ_v with $\gamma_{1|2} = 0$. In the inviscid, magnetostatic, shallow and small β-limit, without surface tension, the model of [10] (same for [9]) rigorously links to our result.

Appendix C: The effect of symmetrical electrical boundary conditions on top and bottom electrodes

The top and bottom boundary conditions (6c) and (6d) for the electrical potential and currents (6c) are well adapted to model metal pad roll instability in Hall-Heroult cells, because they mimic the fact that the top Carbon anodes are well conducting with respect to the Cryolite, that the cathode bottom vessel is a less good conductor than Aluminium. Nevertheless, this is an approximation and we found it interesting to study the impact of using different top and bottom boundary conditions, namely

$$
(\text{zero } \varphi) \qquad \varphi_1|_{z=H_1} = \varphi_2|_{z=-H_2} = 0 \tag{C1a}
$$
$$
(\text{zero } j_z) \qquad j_{1,z}|_{z=H_1} = j_{2,z}|_{z=-H_2} = 0 \tag{C1b}
$$

For these different electrical boundary conditions, we find the potentials
(zero φ)

$$
\begin{bmatrix} \widehat{\varphi}_1 \\ \widehat{\varphi}_2 \end{bmatrix} = \frac{JkA}{\omega} \frac{\sigma_1^{-1} - \sigma_2^{-1}}{\sigma_1^{-1}\tanh(kH_1) + \sigma_2^{-1}\tanh(kH_2)} \begin{bmatrix} -\mathrm{i}\sinh(k(z - H_1))/(\sigma_1\cosh(kH_1)) \\ -\mathrm{i}\sinh(k(z + H_2))/(\sigma_2\cosh(kH_2)) \end{bmatrix} J_m(kr)e^{\mathrm{i}m\theta} \tag{C2a}
$$

(zero j_z)

$$
\begin{bmatrix} \widehat{\varphi}_1 \\ \widehat{\varphi}_2 \end{bmatrix} = \frac{JkA}{\omega} \frac{\sigma_1^{-1} - \sigma_2^{-1}}{\sigma_1^{-1}\tanh^{-1}(kH_1) + \sigma_2^{-1}\tanh^{-1}(kH_2)} \begin{bmatrix} \mathrm{i}\cosh(k(z - H_1))/(\sigma_1\sinh(kH_1)) \\ -\mathrm{i}\cosh(k(z + H_2))/(\sigma_2\sinh(kH_2)) \end{bmatrix} J_m(kr)e^{\mathrm{i}m\theta} \tag{C2b}
$$

in the magneto-static inviscid limit. We then recalculate $\mathcal{P}_v$ and find the growth rate

$$
\lambda_v = \frac{\omega}{2} \frac{JB_z}{(\rho_2 - \rho_1)g + \gamma_{1|2}k^2} \frac{m}{(kR)^2 - m^2} \Lambda \tag{C3}
$$

with

$$
(\text{zero } \varphi) \quad \Lambda = \frac{(\sigma_1^{-1} - \sigma_2^{-1})\left[\tanh(kH_1) + \tanh(kH_2)\right]}{\sigma_1^{-1}\tanh(kH_1) + \sigma_2^{-1}\tanh(kH_2)} \tag{C4a}
$$

$$
(\text{zero } j_z) \quad \Lambda = \frac{(\sigma_1^{-1} - \sigma_2^{-1})\left[(kH_1)\sinh^{-2}(kH_1) + \tanh^{-1}(kH_1) + (kH_2)\sinh^{-2}(kH_2) + \tanh^{-1}(kH_2)\right]}{\sigma_1^{-1}\tanh^{-1}(kH_1) + \sigma_2^{-1}\tanh^{-1}(kH_2)} \tag{C4b}
$$

In the deep limit $kH_i \gg 1$ and for large conductivity jumps $\sigma_1 \ll \sigma_2$, we find that

$$
\lambda_{v,deep} \approx \frac{JB_z}{(\rho_2 - \rho_1)g + \gamma_{1|2}k^2} \frac{m\omega_{deep}}{(kR)^2 - m^2} \tag{C5}
$$

in both alternative boundary condition cases, which is also the exact same formula as (50a). The fact that top and bottom boundary conditions do not have an impact on the growth rate in deep cells is not a surprise: all the motion occurs near the interface, far away from the top and bottom boundaries. In the shallow limit $kH_i \ll 1$ and for large conductivity jumps $\sigma_1 \ll \sigma_2$, we have

$$
(\text{zero } \varphi) \quad \lambda_{v,shallow} \approx \frac{JB_z}{(\rho_2 - \rho_1)g + \gamma_{1|2}k^2} \left[\frac{1}{2}\left(1 + \frac{H_2}{H_1}\right)\right] \frac{m\omega_{shallow}}{\kappa_{mn}^2 - m^2} \tag{C6a}
$$

$$
(\text{zero } j_z) \quad \lambda_{v,shallow} \approx \frac{JB_z}{(\rho_2 - \rho_1)g + \gamma_{1|2}k^2} \left(1 + \frac{H_1}{H_2}\right) \frac{m\omega_{shallow}}{\kappa_{mn}^2 - m^2} \tag{C6b}
$$

These formulas are very different from the shallow-limit formula in the mixed type boundary condition case. Comparing all three cases of top and bottom boundary conditions, we can conclude that the mixed type boundaries, used in the body of the text, always yield the most unstable cells in the shallow limit.

Appendix D: Calculation of viscous effects caused by boundary layers on rigid walls

To find the leading order viscous damping rates, we must account for dissipation in the boundary layer regions that come in 4 different types. We have (1) strong Stokes boundary layers near the rigid walls Σ_i, (2) weak Stokes boundary layers near the interface $\mathcal{S}$, (3) complex boundary layers in corners of the rigid surface Σ_i and 4) very complex (moving) boundary layers near the meniscus $\mathcal{M}$. Damping caused in regions 1 and 2 is straightforward to model, but corners and meniscus regions 3 and 4 are really difficult to deal with and so they are not often considered in theoretical calculations.

Using the (energy-equation) method of [41], [45] calculated the viscous damping of gravity waves in cylinders. This calculation included dissipation caused by boundary layers in regions 1 (strong influence) and 2 (weak influence), but ignored what happens in regions 3 and 4. We have extended this approach to our two-fluid system, but prefer here an alternative approach that better relates to our perturbative framework. This approach better illustrates why it is dangerous to ignore the complex boundary layer structure near the contact line in region 4.

1. First approach : viscosity enters through modifications in the solvability condition

We temporarily skip the use of indices i since both fluid regions are dealt with similarly and this avoids overloaded notation. We focus on the effect of boundary layers in region 1, near rigid walls Σ_i. We extend the asymptotic Ansatz (57) to

$$[\boldsymbol{u} + \overline{\boldsymbol{u}}, p + \overline{p}, \ldots] = \left(\left[\widehat{\boldsymbol{u}} + \widehat{\overline{\boldsymbol{u}}}_i, \widehat{p} + \widehat{\overline{p}}, \ldots \right] + \left[\widetilde{\boldsymbol{u}} + \widetilde{\overline{\boldsymbol{u}}}, \widetilde{p} + \widetilde{\overline{p}}, \ldots \right] \right) e^{(i\omega + \alpha)t} \tag{D1}$$

for the flow and pressure variables. The fields $\widehat{\boldsymbol{u}}, \widehat{p}$ are the inviscid gravity wave profiles. Barred variables designate boundary layer corrections that only exist in $O(\sqrt{\nu/\omega})$ wide boundary layer regions in the immediate vicinity of the rigid walls and the free surface. The corrections are required in order to meet the no-slip condition

$$\boldsymbol{u}|_\Sigma + \overline{\boldsymbol{u}}|_\Sigma = \boldsymbol{0} \tag{D2}$$

In a first step in analysis, we calculate the leading order structure of $\overline{\boldsymbol{u}}|_\Sigma$. Let $\boldsymbol{x}$ be the position vector in the fluid regions, $\boldsymbol{x}_\Sigma$ the position vector of the rigid surface Σ and $\boldsymbol{n}$ the unit outward normal. We introduce a rescaled wall-normal coordinate

$$\zeta = \sqrt{\frac{|\omega|}{\nu}} \left(\boldsymbol{x}_\Sigma - \boldsymbol{x} \right) \cdot \boldsymbol{n} \tag{D3}$$

When the viscosity is low or more precisely when the Reynolds number

$$Re = \frac{|\omega| R^2}{\nu} \gg 1 \tag{D4}$$

is high, this wall normal coordinate ζ is quickly increasing away from the boundaries and inward the fluid. As such, it is well adapted to capture the quick boundary layer variations. We suppose that the wall-normal dependence of boundary layer corrections is entirely carried by ζ (this is only true away from corners and the meniscus). To express the momentum and mass balance in near wall regions, we replace

$$\boldsymbol{\nabla} \cdot \overline{\boldsymbol{u}} \approx \boldsymbol{\nabla}_\perp \cdot \overline{\boldsymbol{u}}_\perp - \sqrt{\frac{|\omega|}{\nu}} \partial_\zeta (\overline{\boldsymbol{u}} \cdot \boldsymbol{n}) \,, \quad \boldsymbol{\nabla} \overline{p} \approx \boldsymbol{\nabla}_\perp \overline{p} - \boldsymbol{n} \sqrt{\frac{|\omega|}{\nu}} \partial_\zeta \overline{p} \,, \quad \boldsymbol{\nabla}^2 \overline{\boldsymbol{u}} \approx \frac{|\omega|}{\nu} \partial^2_{\zeta\zeta} \overline{\boldsymbol{u}} \tag{D5}$$

Here $\perp$ refers to the part of the vector field that is tangential to the boundary and $\overline{u}_n = \overline{\boldsymbol{u}} \cdot \boldsymbol{n}$. Using this and the fact that tilded fields are $O(Re^{-1/2})$ smaller than hatted fields, we get the leading balance

$$\partial_\zeta \widehat{\overline{p}} = 0 \,, \quad \partial_\zeta (\widehat{\overline{\boldsymbol{u}}} \cdot \boldsymbol{n}) = 0 \,, \quad i \operatorname{Sgn}(\omega) \widehat{\overline{\boldsymbol{u}}}_\perp = \partial^2_{\zeta\zeta} \widehat{\overline{\boldsymbol{u}}}_\perp \tag{D6}$$

We can easily solve these equations and using the no-slip condition on the rigid surface, $\widehat{\boldsymbol{u}}|_\Sigma + \widehat{\overline{\boldsymbol{u}}}|_{\zeta=0} = 0$ together with the constraint that boundary layer corrections decay to zero as $\zeta \to +\infty$, we find the leading order boundary layer correction

$$\widehat{\overline{p}} = 0 \,, \quad \widehat{\overline{\boldsymbol{u}}} \cdot \boldsymbol{n} = 0 \,, \quad \widehat{\overline{\boldsymbol{u}}}_\perp = -\widehat{\boldsymbol{u}}_\perp|_\Sigma \exp\left(-\Gamma\zeta\right) \tag{D7}$$

We abbreviate $\Gamma = (1 + \mathrm{i}\,\mathrm{Sgn}(\omega))/\sqrt{2}$. This boundary layer correction produces a small wall-normal flow $\widetilde{\widetilde{\boldsymbol{u}}} \cdot \boldsymbol{n}$ that can be calculated using mass-conservation. We need to have

$$\partial_\zeta(\widetilde{\widetilde{\boldsymbol{u}}} \cdot \boldsymbol{n}) = \sqrt{\frac{\nu}{|\omega|}} \boldsymbol{\nabla}_\perp \cdot \widehat{\widetilde{\boldsymbol{u}}}_\perp \quad \Rightarrow \quad \widetilde{\widetilde{\boldsymbol{u}}} \cdot \boldsymbol{n} = \frac{1}{\Gamma}\sqrt{\frac{\nu}{|\omega|}} \boldsymbol{\nabla}_\perp \cdot \widehat{\boldsymbol{u}}_\perp|_\Sigma \exp\left(-\Gamma\zeta\right) \tag{D8}$$

Expressing impenetrability $\widetilde{\boldsymbol{u}} \cdot \boldsymbol{n}|_\Sigma + \widetilde{\widetilde{\boldsymbol{u}}} \cdot \boldsymbol{n}|_{\zeta=0} = 0$, we then find that

$$\widetilde{\boldsymbol{u}}_i \cdot \boldsymbol{n}_i|_{\Sigma_i} = -\frac{1}{\Gamma}\sqrt{\frac{\nu_i}{|\omega|}} \boldsymbol{\nabla}_\perp \cdot \widehat{\boldsymbol{u}}_{i,\perp}|_{\Sigma_i} \tag{D9}$$

bringing back in the indices $i = 1, 2$ referring to the different fluid regions. This relation has the following meaning: a small inviscid flow (with tildes) is forced in the bulk (without bars) as a reaction to a small mass flux of viscous origin that sprout out from the boundary layers. This phenomenon is usually called "boundary layer pumping".

The viscous modification of the boundary condition enters our perturbative model on metal pad roll instability through the solvability condition (62), more precisely through the boundary terms marked by T_2. In the viscous model, we need to replace

$$T_2 = \alpha\mathcal{K} + \mathcal{D} \tag{D10}$$

where

$$\mathcal{D} = \sum_{i=1,2} \int_{\Sigma_i} \widehat{p}_i^* \widetilde{\boldsymbol{u}}_i \cdot \boldsymbol{n}_i|_{\Sigma_i} \,\mathrm{d}S = -\frac{1}{\Gamma}\sum_{i=1,2}\sqrt{\frac{\nu_i}{|\omega|}} \int_{\Sigma_i} \widehat{p}_i^* \boldsymbol{\nabla}_\perp \cdot \widehat{\boldsymbol{u}}_{i,\perp}|_{\Sigma_i} \,\mathrm{d}S \tag{D11}$$

is the power that is dissipated in the boundary regions near the rigid walls. Let us now express these contributions at the different parts of the boundary and in both fluids. Considering that the flow is potential, so that $\widehat{\boldsymbol{u}}_\perp = \boldsymbol{\nabla}_\perp\widehat{\phi}$ and the fact that $\boldsymbol{\nabla}_\perp^2\widehat{\phi}_i = -k^2\widehat{\phi}_i$ on top and bottom plates, $\boldsymbol{\nabla}_\perp^2\widehat{\phi}_i = (k^2 - m^2/R^2)\widehat{\phi}_i$ on the radial walls, we then have

$$\widetilde{u}_{i,r}|_{r=R} = \frac{1}{\Gamma}\sqrt{\frac{\nu_i}{|\omega|}}(-k^2 + m^2/R^2)\widehat{\phi}_i|_{r=R} \tag{D12a}$$

$$\widetilde{u}_{1,z}|_{z=H_1} = \frac{1}{\Gamma}\sqrt{\frac{\nu_1}{\omega}}k^2\widehat{\phi}_1|_{z=H_1} \tag{D12b}$$

$$-\widetilde{u}_{2,z}|_{z=-H_2} = \frac{1}{\Gamma}\sqrt{\frac{\nu_2}{|\omega|}}k^2\widehat{\phi}_2|_{z=-H_2} \tag{D12c}$$

The power that is dissipated in the boundary layers is then

$$\mathcal{D} = 2\pi R\underbrace{\left[\int_0^{H_1}\widehat{p}_1^*\widetilde{u}_{1,r}|_{r=R}\,\mathrm{d}z + \int_{-H_2}^0\widehat{p}_2^*\widetilde{u}_{2,r}|_{r=R}\,\mathrm{d}z\right]}_{\mathcal{D}_{side}} + 2\pi\underbrace{\int_0^R\widehat{p}_1^*\widetilde{u}_{1,z}|_{z=H_1}\,r\,\mathrm{d}r}_{\mathcal{D}_{top}} + 2\pi\underbrace{\int_0^R\widehat{p}_2^*(-\widetilde{u}_{2,z})|_{z=-H_2}\,r\,\mathrm{d}r}_{\mathcal{D}_{bot}}$$

$$\tag{D13}$$

Physically, we expect that $\mathrm{Re}(\mathcal{D}) \geq 0$, since only then it can yield a damping. Using (D12) and $\widehat{p}_i^* = \rho_i(i\omega)\widehat{\phi}_i^*$, we can now find out how each surface contributes to the dissipated power

$$\mathcal{D}_{side} = -2\pi\Gamma\left(k^2 - \frac{m^2}{R^2}\right)\left[\sqrt{\nu_1|\omega|}\rho_1 R\int_0^{H_1}|\widehat{\phi}_1|_{r=R}|^2\mathrm{d}z + \sqrt{\nu_2|\omega|}\rho_2 R\int_{-H_2}^0|\widehat{\phi}_2|_{r=R}|^2\mathrm{d}z\right] \tag{D14a}$$

$$\mathcal{D}_{top} = 2\pi\Gamma k^2\left[\sqrt{\nu_1|\omega|}\rho_1\int_0^R|\widehat{\phi}_1|_{z=H_1}|^2\,r\,\mathrm{d}r\right] \tag{D14b}$$

$$\mathcal{D}_{bot} = 2\pi\Gamma k^2\left[\sqrt{\nu_2|\omega|}\rho_2\int_0^R|\widehat{\phi}_2|_{z=-H_2}|^2\,r\,\mathrm{d}r\right] \tag{D14c}$$

The contributions from the top and bottom clearly have the right sign, but $\mathcal{D}_{side}$ causes serious troubles. With $k^2 - (m^2/R^2) > 0$, this calculation results in $\mathcal{D}_{side} < 0$ which is very unphysical, but nevertheless a mathematical fact.

The problem we have here finds its origin in the contact line region. If we omit a correct description of boundary layers near the contact line, we can certainly miss some essential terms that can balance the unphysical term $\mathcal{D}_{side}$. We do not want to calculate these complex layers, but we can isolate the problematic contribution in $\mathcal{D}_{side}$ that arises near the meniscus. Using $\widehat{p}_i^* = \rho_i(i\omega)\widehat{\phi}_i^*$ and a partial integration, we transform (D11) into

$$\mathcal{D} = \Gamma \underbrace{\sum_{i=1,2} \rho_i \sqrt{\nu_i|\omega|} \int_{\Sigma_i} |\widehat{\boldsymbol{u}}_{i,\perp}|^2 \mathrm{d}S}_{\mathcal{D}_{reg}} + \underbrace{\Gamma(2\pi R) \left[\rho_1\sqrt{\nu_1|\omega|}\,\widehat{\phi}_1^*\widehat{u}_{1,z} - \rho_2\sqrt{\nu_2|\omega|}\,\widehat{\phi}_2^*\widehat{u}_{2,z}\right]\Big|_{(r,z)=(R,0)}}_{\mathcal{D}_{prob}} \tag{D15}$$

The term $\mathcal{D}_{reg}$ is a well-behaving part that always has $\mathrm{Re}(\mathcal{D}_{reg}) \geq 0$. Under the square brackets of $\mathcal{D}_{reg}$, we recognize a typical measure of kinetic energy in the entire boundary layer region over the solid walls. The term $\mathcal{D}_{prob}$ concentrates all the bad behaving terms and is located in the contact line region $(r,z) = (R,0)$. This contribution would at least be partly canceled by a better modeling of the boundary layer in this region. In absence of a better contact line model, we brutally discard these problematic terms $\mathcal{D}_{prob}$ and keep only the well behaving term $\mathcal{D}_{reg}$ in what follows. This yields a complex frequency shift $\alpha = \lambda_{visc} + i\delta_{visc}$ with

$$\lambda_{visc} = -\frac{\mathrm{Re}(\mathcal{D}_{reg})}{2\mathcal{K}} = -\frac{1}{\sqrt{2}}\sum_{i=1,2}\left\{\frac{\sqrt{\frac{\nu_i|\omega|}{R^2}}\rho_i\left[k(R-H_i)\sinh^{-2}(kH_i) + \left(\frac{k^2R^2+m^2}{k^2R^2-m^2}\right)\tanh^{-1}(kH_i)\right]}{\left[\rho_2\tanh^{-1}(kH_2) + \rho_1\tanh^{-1}(kH_1)\right]}\right\} \tag{D16a}$$

and

$$\delta_{visc} = -\frac{\mathrm{Im}(\mathcal{D}_{reg})}{2\mathcal{K}} = \mathrm{Sgn}(\omega)\, s_{visc} \tag{D16b}$$

that are given in the body of the article.

2. Second approach : viscous damping using the mechanical energy balance

The formula for the viscous damping rate λ_{visc} may alternatively be obtained using the method of [45] and this is briefly demonstrated here. The method of [45] starts from the mechanical energy balance, that is

$$\underbrace{\frac{d}{dt}\left(\sum_{i=1,2}\frac{1}{2}\int_{\mathcal{V}_i}\rho||\boldsymbol{u}_i||^2 dV\right)}_{\mathcal{E}_c} + \underbrace{\frac{d}{dt}\left(\frac{1}{2}\int_S \left((\rho_2-\rho_1)g\eta^2 + \gamma_{1|2}||\boldsymbol{\nabla}^2\eta||\right)\,dS\right)}_{\mathcal{E}_p}$$

$$= -\underbrace{\sum_{i=1,2}\rho_i\nu_i\int_{\mathcal{V}_i}||\boldsymbol{\nabla}\times\boldsymbol{u}_i||^2 dV}_{\mathcal{D}_{visc}} + \underbrace{\sum_{i=1,2}\rho_i\nu_i\int_S \left[(\boldsymbol{\nabla}\times\boldsymbol{u}_i)\times\boldsymbol{u}_i\right]\cdot\boldsymbol{n}_i\,dS}_{\mathcal{D}'_{visc}} \tag{D17}$$

in this problem. This equation can be derived by summing the momentum balances of both fluid regions respectively multiplied with $\boldsymbol{u}_i$ and using all the boundary conditions together with many partial integrations. In the left hand side, we recognize the time-derivative of mechanical energy. In the right hand side, we find viscous dissipation and the surface integral only is relevant near the free interface. Damping there is weak and we will ignore this term in what follows $\mathcal{D}'_{visc} \approx 0$ to lowest order. In this balance, we then inject the flow profiles of a viscously decaying rotating gravity wave

$$\boldsymbol{u}_i \approx \left[\left(\widehat{\boldsymbol{u}}_i + \widehat{\widehat{\boldsymbol{u}}}_i\right)e^{i(\omega+\delta_{visc})t} + c.c.\right]e^{\lambda_{visc}t} \tag{D18}$$

$$\eta \approx \left[\widehat{\eta}\,e^{i(\omega+\delta_{visc})t} + c.c.\right]e^{\lambda_{visc}t} \tag{D19}$$

Here $c.c.$ denotes the "complex conjugated part" . It is crucial to use real-valued flows in this energetic approach, otherwise one can easily get damping rates that are wrong by a factor of two. We calculate the kinetic and potential

energy approximatively by ignoring the boundary layer corrections and find

$$\mathcal{E}_c \approx \left(\sum_{i=1,2} \int_{\mathcal{V}_i} \rho ||\widehat{\boldsymbol{u}}_i||^2 dV \right) e^{2\lambda_{visc}t} = \mathcal{K}e^{2\lambda_{visc}t}$$

$$\mathcal{E}_p \approx \left(\int_S \left((\rho_2 - \rho_1)g|\widehat{\eta}|^2 + \gamma_{1|2}||\boldsymbol{\nabla}^2\widehat{\eta}|| \right) \ dS \right) e^{2\lambda_{visc}t} = \mathcal{K}e^{2\lambda_{visc}t} \tag{D20}$$

We use here the notation $\mathcal{K}$ for the integrals that were previously encountered in the article. Viscous dissipation is located in the boundary layers since only $\widehat{\overline{\boldsymbol{u}}}_i$ carries vorticity, so

$$\mathcal{D}_{visc} \approx -2 \sum_{i=1,2} \rho_i \nu_i \int_{\mathcal{V}_i} ||\boldsymbol{\nabla} \times \widehat{\overline{\boldsymbol{u}}}_i||^2 dV \tag{D21}$$

Using the boundary layer profiles of (D7), one can find that

$$||\boldsymbol{\nabla} \times \widehat{\overline{\boldsymbol{u}}}_i||^2 \approx \frac{|\omega|}{\nu_i} \left||\widehat{\boldsymbol{u}}_{i,\perp}|_{\Sigma_i}\right||^2 \ e^{-\sqrt{2}\zeta} \tag{D22}$$

Here we only include the dominant contributions that arise due to the sharp wall-normal variation of the tangential flow near the walls. Integration over the boundary layer regions (meaning $\zeta \in [0, +\infty[$) yields

$$\mathcal{D}_{visc} \approx -\frac{2}{\sqrt{2}} \sum_{i=1,2} \rho_i \sqrt{\nu_i|\omega|} \int_{\Sigma_i} |\widehat{\boldsymbol{u}}_{i,\perp}|^2 \mathrm{d}S \tag{D23}$$

Comparing with (D15), we can notice that $\mathcal{D}_{visc} = -2\mathrm{Re}(\mathcal{D}_{reg})$. Expressing the energy balance, we find $4\lambda_{visc}\mathcal{K} = \mathcal{D}_{visc}$, and so $\lambda_{visc} = -\mathrm{Re}(\mathcal{D}_{reg})/2\mathcal{K}$ as before. This second method of [45] yields precisely the damping rate (D16a) and certainly is more simple to implement. However, it does not provide the viscous detuning nor does it highlight the problems that can arise near the contact line.

[1] N. Urata, K. Mori, and H. Ikeuchi, WAA Translation from: J. Jpn. Inst. Light Met. **26**, 30 (1976).
[2] T. Sele, Metallurgical and Materials Transactions B **8**, 613 (1977).
[3] A. Sneyd, Journal of Fluid Mechanics **156**, 223 (1985).
[4] R. Moreau and D. Ziegler, Light Metals **2**, 359 (1986).
[5] P. Davidson and R. Boivin, Light Metals , 1199 (1992).
[6] D. Ziegler, Metallurgical and Materials Transactions B **24**, 899 (1993).
[7] A. Sneyd and A. Wang, Journal of Fluid Mechanics **263**, 343 (1994).
[8] V. Bojarevics and M. Romerio, European Journal of Mechanics B Fluids **13**, 33 (1994).
[9] P. Davidson and R. Lindsay, Journal of Fluid Mechanics **362**, 273 (1998).
[10] A. Lukyanov, G. El, and S. Molokov, Physics Letters A **290**, 165 (2001).
[11] S. Molokov, G. El, and A. Lukyanov, Theoretical and Computational Fluid Dynamics **25**, 261 (2011).
[12] O. Zikanov, H. Sun, and D. Ziegler, Light Metals , 445 (2004).
[13] V. Bojarevics and K. Pericleous, Light Metals , 347 (2006).
[14] V. Bojarevics and K. Pericleous, Light metals , 403 (2008).
[15] J.-F. Gerbeau, T. Lelièvre, and C. Le Bris, Journal of Computational Physics **184**, 163 (2003).
[16] J.-F. Gerbeau, T. Lelièvre, and C. Le Bris, Computers & fluids **33**, 801 (2004).
[17] J.-F. Gerbeau, C. Le Bris, and T. Lelièvre, *Mathematical methods for the magnetohydrodynamics of liquid metals* (Clarendon Press, 2006).
[18] D. Severo, A.-F. Schneider, E. Pinto, V. Gusberti, and V. Potocnik, Light Metals **2005**, 475 (2005).
[19] D. Severo, V. Gusberti, A.-F. Schneider, E. Pinto, and V. Potocnik, in *Light Metals*, Vol. 2008 (TMS, 2008) p. 413.
[20] D. Munger and A. Vincent, Magnetohydrodynamics **42**, 417 (2006).
[21] D. Munger and A. Vincent, Journal of Computational Physics **217**, 295 (2006).
[22] M. Flueck, T. Hofer, M. Picasso, J. Rappaz, and G. Steiner, International Journal of Numerical Analysis and Modeling **6**, 489 (2009).
[23] G. Steiner, *Simulation numérique de phénomènes MHD: application à l'électrolyse de l'aluminium*, Ph.D. thesis, École Polytechnique Fédérale de Lausanne (2009).
[24] M. Flueck, A. Janka, C. Laurent, M. Picasso, J. Rappaz, and G. Steiner, Journal of Scientific Computing **43**, 313 (2010).
[25] J.-L. Guermond, R. Laguerre, J. Léorat, and C. Nore, J. Comput. Phys. **221**, 349 (2007).
[26] J.-L. Guermond, R. Laguerre, J. Léorat, and C. Nore, J. Comput. Phys. **228**, 2739 (2009).

[27] C. Nore, D. C. Quiroz, L. Cappanera, and J.-L. Guermond, EPL (Europhysics Letters) **114**, 65002 (2016).

[28] L. Cappanera, J.-L. Guermond, W. Herreman, and C. Nore, International Journal for Numerical Methods in Fluids **86**, 541 (2018).

[29] W. Herreman, C. Nore, L. Cappanera, and J.-L. Guermond, Journal of Fluid Mechanics **771**, 79 (2015).

[30] H. G. Weller, G. Tabor, H. Jasak, and C. Fureby, Comput. Phys. **12**, 620 (1998).

[31] N. Weber, V. Galindo, F. Stefani, T. Weier, and T. Wondrak, New Journal of Physics **15**, 043034 (2013).

[32] N. Weber, V. Galindo, F. Stefani, and T. Weier, Journal of Power Sources **265**, 166 (2014).

[33] N. Weber, P. Beckstein, V. Galindo, M. Starace, and T. Weier, Comput. Fluids **168**, 101 (2018).

[34] R. Ashour, D. H. Kelley, A. Salas, M. Starace, N. Weber, and T. Weier, J. Power Sources **378**, 301 (2018).

[35] N. Weber, P. Beckstein, V. Galindo, W. Herreman, C. Nore, F. Stefani, and T. Weier, Magnetohydrodynamics **53**, 129 (2017).

[36] N. Weber, P. Beckstein, W. Herreman, G. Horstmann, C. Nore, F. Stefani, and T. Weier, Physics of Fluids **29**, 054101 (2017).

[37] G. M. Horstmann, N. Weber, and T. Weier, Journal of Fluid Mechanics **845**, 1–35 (2018).

[38] G. M. Horstmann, M. Wylega, and T. Weier, "Measurement of interfacial wave dynamics in orbitally shaken cylindrical containers using ultrasonic pulse-echo techniques," (2018), under submission.

[39] A. Pedchenko, S. Molokov, J. Priede, A. Lukyanov, and P. Thomas, Europhysics Letters **88**, 24001 (2009).

[40] A. Pedcenko, S. Molokov, and B. Bardet, Metallurgical and Materials Transactions B , 1 (2016).

[41] H. Lamb, New York **43** (1945).

[42] B. Sreenivasan, P. A. Davidson, and J. Etay, Physics of Fluids **17**, 117101 (2005).

[43] H. Sun, O. Zikanov, and D. Ziegler, Fluid Dynamics Research **35**, 255 (2004).

[44] D. Munger and A. Vincent, Metallurgical and Materials Transactions B **37**, 1025 (2006).

[45] K. Case and W. Parkinson, Journal of Fluid Mechanics **2**, 172 (1957).

[46] J. Miles and D. Henderson, Annual Review of Fluid Mechanics **22**, 143 (1990).

[47] M. Reclari, M. Dreyer, S. Tissot, D. Obreschkow, F. M. Wurm, and M. Farhat, Phys. Fluids **26**, 052104 (2014).

[48] O. Zikanov, Physical Review E **92**, 063021 (2015).

[49] V. Bojarevics and A. Tucs, in *Light Metals 2017* (Springer, 2017) pp. 687–692.

[50] S. Molokov, EPL (Europhysics Letters) **121**, 44001 (2018).

[51] O. Zikanov, Theoretical and Computational Fluid Dynamics **32**, 325 (2018).

[52] G. N. Watson, *A treatise on the theory of Bessel functions*, 2nd ed. (Cambridge university press, 1995).